THE JOURNAL OF PHYSICAL CHEMISTRY C
A JOURNAL OF THE AMERICAN CHEMICAL SOCIETY

pubs.acs.org/JPCC Article

How the Size and Density of Charge-Transfer Excitons Depend on Heterojunction's Architecture

Márcio T. do N. Varella,* Ljiljana Stojanović, Van Quan Vuong, Stephan Irle, Thomas A. Niehaus, and Mario Barbatti

Cite This: J. Phys. Chem. C 2021, 125, 5458−5474 Read Online

ACCESS | Metrics & More | Article Recommendations | Supporting Information

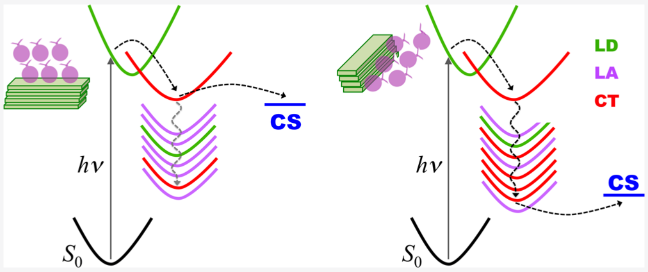

ABSTRACT: We have characterized the size, intensity, density, and distribution of charge-transfer (CT) excitons as a function of the acceptor−donor architecture of prototypical organic interfaces. This characterization was done by computational analysis of 17 models of varying numbers, positions, and orientations of the donor and acceptor molecules. The models' building blocks were phenyl-C_{61}-butyric acid methyl ester (PCBM) fullerene acceptors and dual-band donor polymers composed of thiophene, benzothiadiazole, and benzotriazole subunits. The electronic structure of the donor−acceptor complexes was computed with the time-dependent long-range-corrected density-functional tight-binding method and analyzed with the fragment-based one-electron transition density matrix. In all models, the complexes with edge-on orientation have denser spectra of low-energy CT states lying below the absorption bands compared to the complexes with face-on orientation. This CT-state distribution in edge-on complexes provides a gate to efficiently populate cold CT excitons. Moreover, the cold CT excitons have a higher degree of charge separation in the edge-on than in the face-on complexes. The CT amount and the CT exciton size generally increase with the energy of the CT states, although the electron remains localized on a single molecule in cold CT states. Delocalization over two PCBM molecules was observed for high-energy CT states. The exciton size also depends on the orientation. Larger excitons are produced by the delocalization of the electrons perpendicularly to the interface. When the delocalization is parallel, the smaller electron−hole distances yield moderately sized CT excitons.

1. INTRODUCTION

Efficient charge separation at donor−acceptor (DA) interfaces is critical for the performance of electronic devices. In organic solar cells (OSCs), light absorption typically gives rise to bound excitons, and their dissociation into charge-separated (CS) states can be significantly constrained by radiative and nonradiative recombination processes.[1,2] Charge-transfer (CT) excitons at the interface between donor and acceptor domains have attracted considerable attention in recent years,[3−7] since they are believed to mediate the long-range charge separation in OCSs. Despite the outstanding progress in conversion efficiency,[8−11] the mechanisms for free-carrier production are still under debate. For instance, the generation of free charges from high-energy (hot) CT excitons has been pointed out,[12−14] but significant yields have also been reported for light absorption at subexcitation energies.[15,16] The dissociation mechanisms of interfacial CT excitons, having binding energies ∼10 times higher than ambient thermal energies,[1,15] are also currently in discussion. Several physical effects can impact the exciton dissociation dynamics, such as entropy,[6,17−19] vibronic couplings,[19−22] energy offset,[5,22−31] disorder,[32−36] hybridization between CT and localized states,[7,22,37−39] and also electronic delocalization and polarization,[14,34,40−50] among others.

A number of recent studies have addressed the microscopic structures of the DA interfaces and their impact on free-carrier generation.[5−7,34,38,46,47,51−54] While atomistic simulations can provide invaluable mechanistic and structure−property insights, the importance of going beyond minimal (bimolecular) interface models has been emphasized.[34,47,52,54] Therefore, the computational methods are challenged by the size of the DA heterojunction models, by the need to account for different interface geometries and also by the disorder and finite-temperature effects. The balance between the numerical effort and accuracy is a prominent issue, but the analysis of the excited states of complex molecular systems should not be overlooked. The inspection of molecular orbitals is often tedious and sometimes ineffective in assigning the CT

Received: December 1, 2020
Revised: January 27, 2021
Published: March 3, 2021

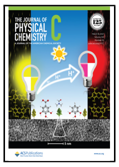

https://dx.doi.org/10.1021/acs.jpcc.0c10762
J. Phys. Chem. C 2021, 125, 5458−5474

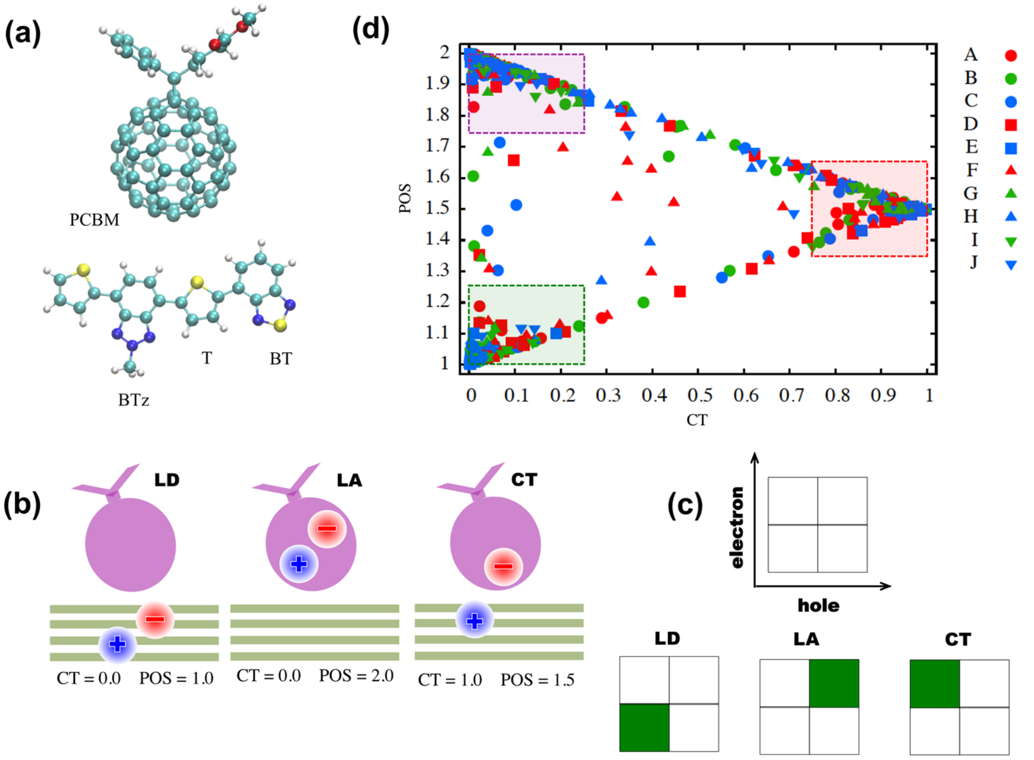

Figure 1. (a) Structures of PCBM and PTBTBTz monomers, with the T, BT, and BTz subunits indicated for the latter. The sulfur atoms are represented in yellow, oxygen in red, nitrogen in deep blue, carbon in light blue, and hydrogen in white. (b) Ideal excited states: Frenkel exciton localized on the donor domain (LD); Frenkel exciton localized on the acceptor domain (LA); and charge-transfer (CT) exciton. In the three panels, the electron and hole locations are indicated by the negative (red) and positive (blue) signs. The values of the CT and POS descriptors for the ideal excitations are also given in the panels, according to eqs 4 and 6. The donor and acceptor positions are defined as 1 and 2, respectively. (c) Electron−hole correlation plots for the ideal LD, LA, and CT excited states, according to eq 3. The electron and hole axes are also shown. (d) CT and position (POS) descriptors for the excited states of several complexes, where the lowest-lying 50 excited states were calculated in each case. The model systems are (A) (dim-PT)$_2$:(PCBM@bt)$_1$:*f*; (B) (dim-PT)$_2$:(PCNM@btz)$_1$:*f*; (C) (dim-PT)$_2$:(PCBM@t)$_1$:*f*; (D) (dim-PT)$_2$:(F@bt)$_1$:*e*; (E) (dim-PT)$_2$:(PCBM@t)$_1$:*e*; (F) (dim-PT)$_3$:(PCBM@bt)$_1$:*f*; (G) (dim-PT)$_3$:(PCBM@btz)$_1$:*f*; (H) (dim-PT)$_3$:(PCBM@t)$_1$:*f*; (I) (dim-PT3)$_2$:(PCBM@btz)$_1$:*f*; and (J) (dim-PT3)$_2$:(PCBM@t)$_1$:*f*. The shaded areas highlight the practical definitions of LD (green), LA (purple), and CT (red) excitons.

character of electronic states, for example, when many electron−hole pairs have significant weights in a given excited state or for systems having multiple chromophores.

In this work, we address the CT excitons of polymer/fullerene complexes combining the time-dependent long-range-corrected density-functional tight-binding (TD-LC-DFTB) method[55−57] with the fragment-based analysis of the calculated excited states.[58−60] The fragmentation into subsystems has proved to be a useful tool to assign, quantitatively and unambiguously, the CT character of exciton states. Its application to DA heterojunctions is particularly appealing since the interface can be viewed as composed of donor and acceptor fragments, which can be further decomposed into oligomer and fullerene fragments. The methodology is applied to model complexes in which the acceptor domains are composed of phenyl-C$_{61}$-butyric acid methyl ester (PCBM) and the donor domains of PTBTBTz, a copolymer composed of thiophene (T), benzothiadiazole (BT), and benzotriazole (BTz) subunits, as shown in Figure 1a. PTBTBTz is an example of D−A$_1$−D−A$_2$ dual-band polymers,[61] which have been considered for application in photovoltaics[61−64] and organic electronics.[65,66] Those copolymers are characterized by bright excitations from the donor subunit (T in the present case) to the strong and weak acceptor subunits (BT and BTz)—the latter acceptor subunits in the PTBTBTz donor domain should not be confused with the acceptor domains of the DA complexes.

The PTBTBTz/PCBM system is an interesting model for our purposes because (i) in addition to cold and hot CT excitons, the dual-band character is expected to give rise to interband CT states; (ii) the relationship between the complex geometry and CT states can be affected by the two absorption bands arising from the electron transfer to two distinct polymer subunits; and (iii) the BT and BTz acceptor subunits are moderately sized compared to those employed in other D−A$_1$−D−A$_2$ polymers,[61] thus helping to manage the computational effort. We explored 17 DA complexes of different sizes and geometries obtained from both geometry optimizations and room-temperature molecular dynamics (MD) simulations. The excited-state analysis employed different fragmentation schemes and exciton properties to draw, as much as possible, general conclusions not restricted to the properties of the PTBTBTz/PCBM system. We explore the edge-on and face-on orientations of the DA domains, which are known to correlate with the device performance,[6,47,51,52] different closest-approach positions of the acceptor molecules along the donor chains, and also the size of the domains. The fragment-based analysis is further applied to physical properties expected to affect the excited-state dynamics, such as the degree of CT, delocalization of the CT excitons, and the electron−hole distances.

2. METHODS

The excitation spectra were calculated with the TD-LC-DFTB method, described in detail elsewhere,[55,57] as implemented in the DFTB+ code.[67] From the formal standpoint, the approach is similar to linear-response time-dependent density functional theory (TD-DFT), that is, one has to solve the generalized eigenvalue equation

$$\begin{bmatrix} \mathbf{A} & \mathbf{B} \\ \mathbf{B}^* & \mathbf{A}^* \end{bmatrix} \begin{bmatrix} \mathbf{X} \\ \mathbf{Y} \end{bmatrix} = \Omega \begin{bmatrix} \mathbf{1} & \mathbf{0} \\ \mathbf{0} & -\mathbf{1} \end{bmatrix} \begin{bmatrix} \mathbf{X} \\ \mathbf{Y} \end{bmatrix} \tag{1}$$

where the **A** and **B** matrices are given by

$$\begin{aligned} A_{ia\sigma,jb\sigma'} &= \delta_{ij}\delta_{ab}\delta_{\sigma\sigma'}(\varepsilon_{a\sigma} - \varepsilon_{i\sigma}) + (ia\sigma||jb\sigma') \\ B_{ia\sigma,jb\sigma'} &= (ia\sigma||bj\sigma') \end{aligned} \tag{2}$$

In the expressions mentioned above, Ω denotes the excitation energies (eigenvalues), $\varepsilon_{i\sigma,a\sigma}$ are orbital energies obtained from a previous ground-state calculation for spin σ, and $(ia\sigma||ja\sigma')$ are generalized electron repulsion matrix elements, which involve occupied (i, j) and virtual (a, b) orbitals, and account for the Hartree and exchange−correlation interactions. In TD-LC-DFTB, the two-electron integrals are computed with a Mulliken approximation to increase the numerical efficiency.[68]

The TD-LC-DFTB method is built on the LC-DFTB counterpart. The Coulomb interaction is split into short- and long-range components using a Yukawa ansatz,[55] and the DFTB approximation for the short-range contribution is obtained from the Baer, Neuhauser, and Livshits (BNL) exchange−correlation functional.[69,70] A second-order expansion of the Kohn−Sham total energy around a reference density matrix is carried out, $\rho = \rho_0 + \delta\rho$, where ρ_0 is the sum of BNL atomic density matrices. While we do not discuss the approximations employed to obtain the DFTB ground-state energies,[71] we mention the decomposition of the total energy into two contributions, $E_{\text{total}} = E_{\text{el}} + E_{\text{rep}}$. The electronic part, E_{el}, involves the computation of the Hamiltonian matrix elements, which only depend on the reference density. The corresponding diagonal elements are given by the atomic orbital energies, while the off-diagonal elements are precomputed for pairs of elements over a range of internuclear distances, along with the overlap matrix and the repulsive energy component. These precomputed values are tabulated in the Slater−Koster (SK) files.[71] The electronic part further accounts for deviations from the reference density through a charge−charge interaction term.

An SK parametrization with the range-separation parameter $\omega = 0.3a_0^{-1}$, referred to as the OB2 set, was recently reported for the H, C, N, and O elements.[72] The present calculations used re-parametrization of this OB2 set, which includes sulfur and was optimized for five different values of the range-separation parameter, namely, ω = 0.1, 0.2, 0.3, 0.4, and $0.5a_0^{-1}$. The parameter sets used in this work are deposited in the Supporting Information. The inclusion of sulfur is essential for applications in organic electronics, and the range of ω values allows for partial tuning of range separation, which is considered important to describe CT excitations.[4] The complete re-parameterization of the OB2 set will be published elsewhere in the near future.

Our LC-DFTB and TD-LC-DFTB calculations included dispersion interactions via the Slater−Kirkwood model.[73] The ground-state molecular dynamics (MD) simulations were based on LC-DFTB energies and gradients either in the *NVE* or *NVT* ensemble. In the latter case, the Andersen thermostat, built in the DFTB+ code, was employed, with a reselection probability of 0.2. We did not account for the dielectric environment since continuum solvation models are currently not available in the DFTB+ package. A similar study of polymer/fullerene (P3HT/PCBM) interfaces[52] pointed out that accounting for the dielectric medium essentially gives rise to a systematic shift of the excitation spectra, not significantly affecting the photophysics. We expect that the lack of a solvation model should not affect the main conclusions of the present work, as they rely only on the relative energies of the excited states. Finally, the range-separation parameter was set to $\omega = 0.2a_0^{-1}$ for the PTBTBTz/PCBM complexes. This value was chosen because it provided, among the available ω values, the smallest $|\text{IP} - (E^+ - E^0)|$ differences (in absolute value), where E^+ and E^0 are the energies of the cationic and neutral species, respectively, and IP is the ionization potential of the latter.

Other supramolecular models of interest for organic electronics have been recently investigated using an alternative version of TD-LC-DFTB.[56,74−76] In addition to a different parametrization, that version also differs from the present one by not including Hartree−Fock exchange in the DFTB zeroth-order Hamiltonian (see ref 57). In a nonadiabatic dynamic study of a pentacene/fullerene complex based on that TD-LC-DFTB version, Darghouth and co-workers[74] have proposed a value for ω, $0.07a_0^{-1}$, significantly smaller than those used in our simulations.

The exciton analysis employed the recently developed[77] interface between the DFTB+[67] and TheoDORE[78] codes. The latter is a toolbox for the fragment-based analysis of excited states,[60] exploring the one-electron transition density matrix (1-TDM) between the ground and the *I*-th excited state, $\gamma^{0I}(\mathbf{r}_e, \mathbf{r}_h)$, where the electron and hole coordinates are indicated as $\mathbf{r}_{e,h}$. Groups of atoms belonging to the system of interest define molecular fragments. A CT number, for fragments *A* and *B*, can be obtained from the 1TDM by restricting the integrations over the electron and hole coordinates to the *A* and *B* fragments, respectively

$$\Omega_{AB} = \int_A d\mathbf{r}_h \int_B d\mathbf{r}_e \gamma_{0I}{}^2(\mathbf{r}_e, \mathbf{r}_h) \tag{3}$$

Ω_{AB} gives the probability to find the hole on fragment *A*, with the electron in fragment *B*, and it can be evaluated by resorting to a population analysis procedure.[58,60] The interpretation of Ω_{AB} as a matrix defines the electron−hole correlation plots and allows for the definition of several excited-state descriptors.[58] The CT number is obtained from the off-diagonal elements

$$\text{CT} = \frac{1}{\Omega} \sum_A \sum_{B \neq A} \Omega_{AB} \tag{4}$$

with $\Omega = \sum_{A,B} \Omega_{AB}$, and it ranges from CT = 0 (ideal Frenkel exciton) to CT = 1 (ideal charge-transfer exciton). In case the fragments can be arranged along some direction, such that an ordering like *A* = 1, *B* = 2, and so forth can be meaningfully assigned, the position descriptor (POS) for the hole (h) and electron (e) orbitals can be computed as

Table 1. Lowest-Lying Excited States of the PTBTBTz Monomer and the $\mathrm{PTBTBTz_2}$ Stacked Dimer[a]

system	Method		S_1	S_2	S_3	S_4	S_5
PTBTBTz	TD-CAMB3LYP//	E	3.017	3.596	4.308	4.530	4.579
	B3LYP	f	1.022	0.227	0.023	0.015	0.036
	TD-LCwPBE//	E	3.378	4.011	4.740	4.878	4.993
	B3LYP	f	1.219	0.103	0.136	0.095	0.007
	TD-ωB97XD//	E	2.917	3.531	4.382	4.465	4.530
	B3LYP	f	1.121	0.172	0.038	0.009	0.048
	TD-LC-DFTB//	E	2.997	3.639	3.842	4.192	4.201
	B3LYP	f	1.254	0.200	0.000	0.119	0.000
	TD-ωB97XD//	E	3.097	3.670	4.538	4.583	4.651
	ωB97XD	f	1.084	0.180	0.043	0.013	0.060
	TD-LC-DFTB//	E	3.195	3.796	3.957	4.290	4.294
	ωB97XD	f	1.187	0.219	0.000	0.038	0.099
	TD-LC-DFTB//	E	3.351	4.001	4.297	4.520	4.549
	LC-DFTB	f	1.394	0.070	0.000	0.000	0.031
system	method		S_1	S_{B1}	S_{B2}	S_{B3}	S_{B4}
$\mathrm{PTBTBTz_2}$	TD-ωB97XD//	E	2.852	3.133	3.544	3.656	4.725
	ωB97XD	f	0.067	1.247	0.441	0.170	0.266
	TD-LC-DFTB//	E	3.049	3.262	3.472	3.564	3.799
	ωB97XD	f	0.095	1.380	0.177	0.111	0.343
	TD-LC-DFTB//	E	3.204	3.444	4.049	4.559	4.713
	LC-DFTB	f	0.043	2.247	0.169	0.121	0.165

[a] For the monomer, we consider the five lowest-lying excited states, S_1 to S_5, while for the dimer, S_1 and the four lowest-lying bright states, S_{B1} to S_{B4}. The energies, E (in eV), and the oscillator strengths, f, were obtained by several methods. TD-M1//M2 indicates that the excited states were calculated with the time-dependent method M1 at the ground-state geometry optimized with method M2. All DFT and TD-DFT calculations were performed with the 6-31G* basis set.

$$\mathrm{POS_h} = \Omega^{-1}\sum_{A} A\left(\sum_{B} \Omega_{AB}\right)$$

$$\mathrm{POS_e} = \Omega^{-1}\sum_{B} B\left(\sum_{A} \Omega_{AB}\right) \tag{5}$$

with the exciton position given by

$$\mathrm{POS} = \frac{1}{2}(\mathrm{POS_h} + \mathrm{POS_e}) \tag{6}$$

Ideal Frenkel excitons localized on the donor (LD) and on the acceptor (LA) are represented in Figure 1b, along with an ideal CT exciton. The CT and POS descriptors for these excited states are also indicated, and the corresponding electron−hole correlation plots are shown in Figure 1c. The POS descriptor is calculated with the convention $D = 1$ and $A = 2$ for the positions of the donor and acceptor, respectively, whenever the system is decomposed into two fragments.

The 1TDM can also be interpreted as the exciton wave function,[59] $\chi_{\mathrm{exc}}(\mathbf{r}_{\mathrm{e}}, \mathbf{r}_{\mathrm{h}})\!: = \gamma^{0I}(\mathbf{r}_{\mathrm{e}}, \mathbf{r}_{\mathrm{h}})$, which allows for the definition of the exciton size as the root-mean-square (rms) distance between the hole and the electron

$$d_{\mathrm{exc}}{}^{2} = \frac{\langle \chi_{\mathrm{exc}}|(\mathbf{r}_{\mathrm{h}} - \mathbf{r}_{\mathrm{e}})^2|\chi_{\mathrm{exc}}\rangle}{\langle \chi_{\mathrm{exc}}|\chi_{\mathrm{exc}}\rangle} \tag{7}$$

The rms distance can be approximately evaluated by defining atomic pairs, breaking the integrals into atomic volumes, and assuming the electron−hole distance to be equal to the distance between the nuclei (d_{MN}) for each atomic pair[59]

$$d_{\mathrm{exc}} \approx \sqrt{\frac{1}{\Omega}\sum_{M,N} \Omega_{MN} d_{MN}{}^{2}} \tag{8}$$

where Ω_{MN} is the Ω matrix, given in eq 3, for the single-atom fragments M and N.

Figure 1d shows the CT and POS descriptors for the 50 lowest-lying singlet excited states of 10 complexes out of those considered in the present study. The systems were decomposed into two fragments, corresponding to the donor (D) and acceptor (A) domains, and the POS descriptors were calculated with the positions of the D and A fragments chosen as 1 and 2, respectively (see eqs 5 and 6). The data points are somewhat scattered, making the assignment of Frenkel and CT excitons arbitrary to some extent. Nevertheless, most of the points lie close to the corners of a triangle whose vertices correspond to the ideal exciton characters, namely, LD (CT = 0.0, POS = 1.0), LA (CT = 0.0, POS = 2.0), and CT (CT = 1.0, POS = 1.5). We, therefore, employ the following practical definitions

$$\text{LD exciton} = \begin{cases} 0 \le \mathrm{CT} \le 0.25 \\ 1.00 \le \mathrm{POS} \le 1.25 \end{cases} \tag{9}$$

$$\text{LA exciton} = \begin{cases} 0 \le \mathrm{CT} \le 0.25 \\ 1.75 \le \mathrm{POS} \le 2.00 \end{cases} \tag{10}$$

$$\text{CT exciton} = \begin{cases} 0.75 \le \mathrm{CT} \le 1.00 \\ 1.35 \le \mathrm{POS} \le 1.65 \end{cases} \tag{11}$$

and also assign those not matching the abovementioned definitions as mixed-character (MX) excitons. Although we explore different fragmentation schemes, the interfacial CT excitons are always defined using only two fragments corresponding to the D and A domains.

3. RESULTS

Before we discuss the models for PTBTBTz/PCBM interfaces, we comment on the quality of the TD-LC-DFTB calculations compared to the TD-DFT counterparts. Table 1 presents the excitation energies and oscillator strengths for five lowest-energy excited states, S_1 to S_5, of the PTBTBTz monomer (Figure 1a) and the stacked dimer, PTBTBTz$_2$ (the latter is shown in Supporting Information, Figure S1). The DFT and TD-DFT computations were performed with the Gaussian09 package[79] employing different exchange−correlation functionals, standard values for the range-separation parameters, and the 6-31G* basis set. For PBTBTz and PBTBTz$_2$, the TD-LC-DFTB range-separation parameter was set to $\omega = 0.3a_0^{-1}$, based on the same criterion that was described in Section 2. We first compare the excitation spectrum of the PTBTBTz monomer obtained with CAM-B3LYP, LC-ωPBE, ωB97XD, and TD-LC-DFTB, at the ground-state geometry optimized with the B3LYP functional. There is a good agreement ($\lesssim$0.1 eV) between the CAM-B3LYP and ωB97XD excitation energies, while LC-ωPBE overestimates them by ≈0.4 eV with respect to the other functionals. The discrepancies between TD-LC-DFTB energies and those obtained with CAM-B3LYP and ωB97XD vary more significantly from state to state, being mostly around ≈0.1 to ≈0.3 eV, although larger for the S_3 state, ≈0.5 eV. The agreement between TD-LC-DFTB and ωB97XD is similar at the ground-state geometry optimized with the latter functional, although there is some improvement when we compare the excitation energies computed at the respective optimal geometries ($\lesssim$0.4 eV discrepancies). For the PTBTBTz$_2$ dimer, the discrepancies between the TD-ωB97XD and TD-LC-DFTB energies are somewhat lower, in spite of the less favorable agreement for the S_1 state.

The dual-band character of the PTBTBTz polymer is already evident in the monomer. As discussed elsewhere,[61] the bright S_1 and S_2 states mainly arise from excitations out of the T subunit to the BT and BTz subunits, respectively. The oscillator strengths calculated with the TD-DFT and TD-LC-DFTB methods are consistent, with $f \approx 1$ and $f \approx 0.1$ for the transitions to the S_1 and S_2 states, respectively. The situation is similar for the dimer, although with larger differences in the magnitudes of the oscillator strengths, especially when TD-LC-DFTB and TD-ωB97XD are compared at their respective optimal geometries. Particularly at regions where the excited-state spectra are denser, the oscillator strengths, and even the character of the excited states, should be more strongly dependent on the geometry. To further inspect this aspect, we calculated the absorption spectrum of the monomer by performing a Monte Carlo integration of the Wigner distribution function of the vibrational ground state.[80] The simulated spectra, shown in the Supporting Information (Section S-II), were calculated with the Newton-X code[81,82] using the excitation energies, oscillator strengths, and vibrational normal modes obtained with the TD-ωB97XD and TD-LC-DFTB methods. The shapes of the absorptions bands and the overall magnitudes of the cross sections are in good agreement, despite the ≈0.2 eV shift between the maxima of the first bands, which could be anticipated from the vertical excitations reported in Table 1.

The excited states for a minimal PBTBTz/PCBM complex were computed with the TD-LC-DFTB and TD-ωB97XD/6-31G* methods at the ground-state geometries optimized with LC-DFTB and DFT-ωB97XD/6-31G*, respectively. The range-separation parameters were tuned, in the TD calculations, to $\omega = 0.3$ (TD-LC-DFTB) and $\omega = 0.14$ (TD-ωB97XD/6-31G*). The results are shown in Figure 2, where the LD, LA, CT, and MX excitons defined in 9, 10, and 11 are indicated, along with approximate absorption cross sections, in arbitrary units. The latter corresponds to the vertical spectra broadened with Gaussian profiles having a full width at half maxima of 0.1 eV and vertical oscillator strengths corresponding to their area. In general, the TD-LC-DFTB spectrum is blue-shifted by ≈0.3 eV, and the two lowest-lying absorption bands obtained from the TD-ωB97XD/6-31G* calculation, at ≈3.0 and ≈3.4 eV, merge into a single stronger band in the TD-LC-DFTB results. However, the photophysics expected from both models would be similar since the bottom of the spectra has high densities of LA states with a single CT state lying ≈0.2 eV below the brightest states. The comparison between TD-LC-DFTB and the TD-ωB97XD/6-31G* model, largely employed in atomistic models for OSCs, is encouraging. While the TD-LC-DFTB excitation energies are overestimated, the relative energies between the LD, LA, and CT should be more relevant to the excited-state dynamics. Several features of the present results are consistent with TD-DFT computations for DA interfaces,[46,47,52,52] as discussed below. The efficiency of the TD-LC-DFTB method is important since we consider 17 systems with 252 to 340 atoms, amounting to 127 geometries obtained from optimization or MD simulations, and we further explore 8 models with 364 to 412 atoms. Even the larger complexes, however, should be viewed as molecular models not expected to describe the spectra of solid-state systems.

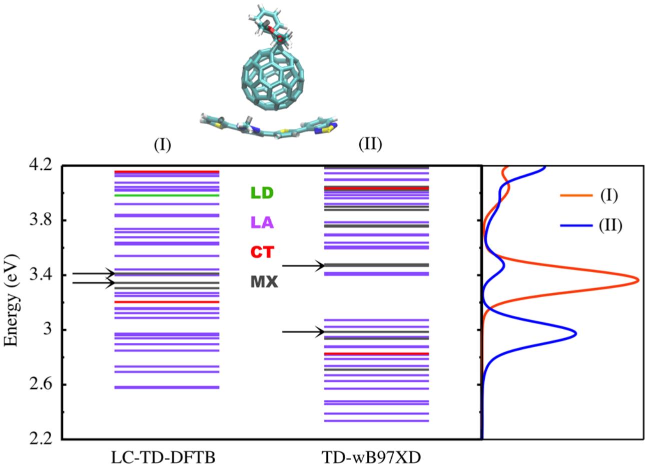

Figure 2. Main panel shows the vertical excitation spectra for the PTBTBTz/PCBM dimer obtained with the (I) TD-LC-DFTB and (II) TD-ωB97XD/6-31G* methods at their respective ground-state stationary geometries. The LD states are indicated in green, LA in purple, CT in red, and MX in gray. The horizontal arrows indicate the low-energy bright transitions. The right panel shows the absorption cross section (in arbitrary units) obtained from the broadening of the vertical spectra with Gaussian line shapes.

The structures of the DA complexes, with varying compositions and conformations, are presented in Figure 3 and in Supporting Information, Figures S2 and S3. Their Cartesian coordinates are also given in the Supporting Information. The donor domains are formed by stacked PTBTBTz oligomers in most cases, although we have

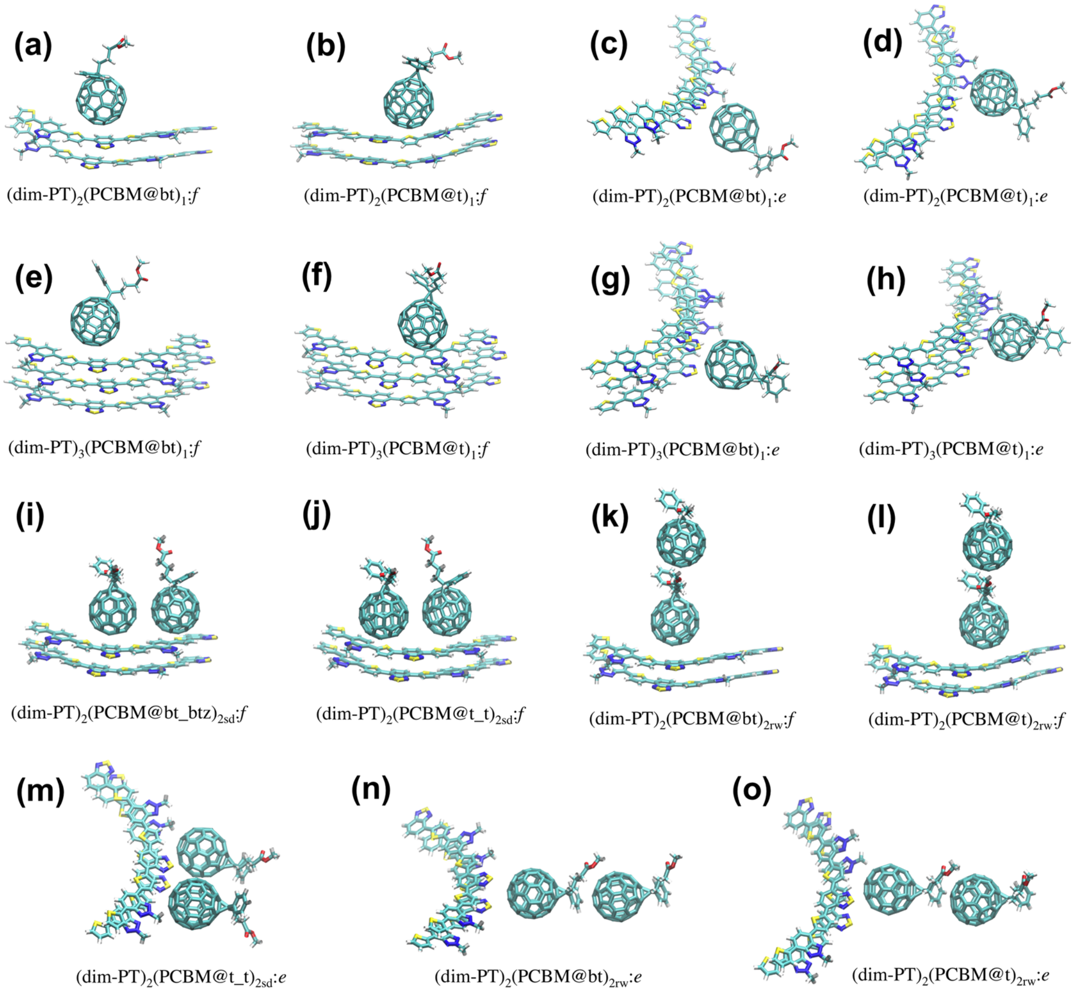

(a) $(\text{dim-PT})_2(\text{PCBM@bt})_1{:}f$
(b) $(\text{dim-PT})_2(\text{PCBM@t})_1{:}f$
(c) $(\text{dim-PT})_2(\text{PCBM@bt})_1{:}e$
(d) $(\text{dim-PT})_2(\text{PCBM@t})_1{:}e$
(e) $(\text{dim-PT})_3(\text{PCBM@bt})_1{:}f$
(f) $(\text{dim-PT})_3(\text{PCBM@t})_1{:}f$
(g) $(\text{dim-PT})_3(\text{PCBM@bt})_1{:}e$
(h) $(\text{dim-PT})_3(\text{PCBM@t})_1{:}e$
(i) $(\text{dim-PT})_2(\text{PCBM@bt\_btz})_{2sd}{:}f$
(j) $(\text{dim-PT})_2(\text{PCBM@t\_t})_{2sd}{:}f$
(k) $(\text{dim-PT})_2(\text{PCBM@bt})_{2rw}{:}f$
(l) $(\text{dim-PT})_2(\text{PCBM@t})_{2rw}{:}f$
(m) $(\text{dim-PT})_2(\text{PCBM@t\_t})_{2sd}{:}e$
(n) $(\text{dim-PT})_2(\text{PCBM@bt})_{2rw}{:}e$
(o) $(\text{dim-PT})_2(\text{PCBM@t})_{2rw}{:}e$

Figure 3. (a) Structures of the complexes addressed in the present study (the remaining structures are shown in the Supporting Information, Figures S2 and S3). In all panels, the donor domain is composed of stacked PTBTBTz dimers, $(\text{dim-PT})_n$, with $n = 3$ stacked chains in panels (e–h) and $n = 2$ stacked chains in the other panels. A single PCBM molecule forms the acceptor domain in panels (a–h). Its relative position, defined by the closest-lying donor subunit, is indicated as $(\text{PCBM@}p)_1$, where p = t (thiophene) in panels (b,d,f,h), and p = bt (benzothiodiazole) in panels (a,c,e,g). The orientation of the PCBM subunits is either face-on, $(\text{PCBM@}p)_1{:}f$, as in panels (a,b,e,f), or edge-on, $(\text{PCBM@}p)_1{:}e$, as in panels (c,d,g,h). In panels (i–o), the acceptor domain is formed by two PCBM molecules, either arranged side-by-side (2sd), as in panels (i,j,m), or in a row (2rw), as in panels (k,l,n,o). The positions are denoted $(\text{PCBM@}p_1\_p_2)$, with $p_1\_p_2$ = t_t, panels (j) and (m), and $p_1\_p_2$ = bt_btz, panel (i), where btz indicates the benzotriazole donor subunit.

performed a few calculations with PT3BTBTz, which has also been considered for OSCs.[61] In the latter, the BT and BTz subunits are intercalated by three T subunits, as shown in Supporting Information, Figure S1. A donor formed by n stacked chains of PTBTBTz or PT3BTBTz oligomers is denoted $(n_{\text{mon}}\text{-PT})_n$ or $(n_{\text{mon}}\text{-PT3})_n$, respectively, where n_{mon} = dim, tri, and tet, respectively, for dimers, trimers, and tetramers, while $n = 2, 3$. The acceptor domains are composed of either one or two PCBM molecules, and we consider their position and orientation with respect to the donor. For a single PCBM molecule, the position is defined by the closest-lying donor subunit (T, BT, or BTz), while the orientations are face-on (f) or edge-on (e) with respect to the stacked oligomers. The complexes are thus denoted $(n_{\text{mon}}\text{-PT})_n(\text{PCBM@}p)_1{:}o$, where p = bt, btz, or t indicates the position (donor subunit lying the closest to the PCBM molecule), while $o = f$, e indicates the orientation. In case two PCBM subunits are present, they may be arranged side-by-side (2sd) or in a row (2rw). The models are therefore denoted $(n_{\text{mon}}\text{-PT})_n(\text{PCBM@}p)_{2rw}{:}o$ and $(n_{\text{mon}}\text{-PT})_n(\text{PCBM@}p_1\_p_2)_{2sd}{:}o$, with $p_1\_p_2$ = t_t, bt_btz.

The excited states of complexes formed by $n = 2$ stacked PTBTBTz dimers and a single PCBM molecule with a face-on orientation are shown in Figure 4a, where the colors indicate the LD, LA, CT, and MX excitons defined in 9, 10, and 11. The excitation spectra were obtained from stationary structures, as described in the Supporting Information (Section S-II), and approximate absorption cross sections are also shown. The face-on models have similar features regardless of the positions (p = bt, t, or btz) of the PCBM molecule. As shown in Table 2, there are two low-lying absorption bands at ≈2.5 and ≈2.8 eV with oscillator strengths around $f \approx 2$ and $f \approx 1$, respectively (in case nearly degenerate states contribute to a given band, we refer to the sum of their strengths). For p = bt or t, the bright states have LD character, although MX character for p = btz. For the three systems, a significant density of LA states is found at the bottom of the bands, that is, lying below the first bright state ($E \lesssim 2.55$ eV). Only a few CT excitons are found either below the first bright state, close

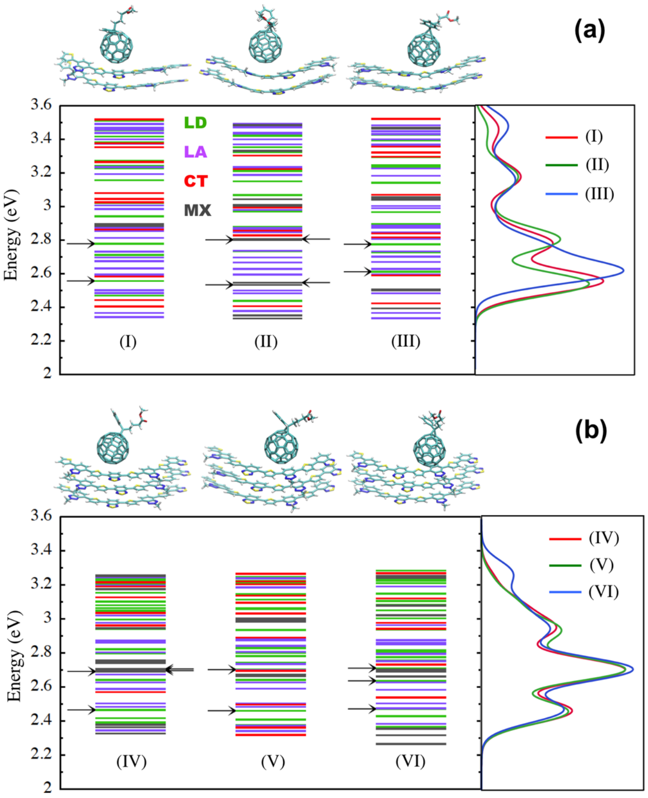

Figure 4. (a) Main panel shows the vertical excitation spectra for the (dim-PT)$_2$:(PCBM@bt)$_1$:*f* (I), (dim-PT)$_2$:(PCBM@btz)$_1$:*f* (II), and (dim-PT)$_2$:(PCBM@t)$_1$:*f* (III) systems. The LD states are indicated in green, LA in purple, CT in red, and MX in gray. The horizontal arrows point to the brightest transitions, and the geometries of the model systems are shown on top of the spectra. The right panel shows the absorption cross section (in arbitrary units) obtained from the broadening of the vertical spectra with Gaussian line shapes. (b) Same as in panel (a) for the (dim-PT)$_3$:(PCBM@bt)$_1$:*f* (I), (dim-PT)$_3$:(PCBM@btz)$_1$:*f* (II), and (dim-PT)$_3$:(PCBM@t)$_1$:*f* (III) systems.

to the second bright state ($E \approx 2.8$ eV), and between these two bright states (2.55 eV $\lesssim E \lesssim$ 2.75 eV).

The models with $n = 3$ stacked PTBTBTz dimers and one PCBM with a face-on orientation, shown in Figure 4b, have denser spectra of LD states, as expected. Once more, the excited states were calculated for stationary structures, with no important differences arising from the different positions (p = bt, btz, or t) of the acceptor with respect to the donor (see also Table 2). The cross sections show an absorption band around 2.9 eV, not present in the models with $n = 2$ stacking (Figure 4a), in addition to the bands around 2.5 and 2.7 eV. The second band has the strongest optical coupling for the $n = 3$ models, with bright states having either LD or MX character. Despite the differences in the absorption cross sections, the n = 2, 3 stacking models mostly have high-energy CT states, with only a few of such states lying around and below the brightest band.

The spectra of the n = 2, 3 stacking models with an edge-on orientation are shown in Figure 5 for the PCBM positions p = bt or t. As described in the Supporting Information (Section S-I), we performed MD simulations before obtaining the stationary structures. The edge-on models with p = btz positions sometimes dissociated along the dynamics, so we did not consider interfaces combining p = btz and o = e. The absorption cross sections for the models with different orientations (o = f, e) but same stacking are fairly similar, since the bright states mostly have an LD character (see Figures 4 and 5, and Table 2). However, the density of low-energy CT excitons is higher for the edge-on orientation, and this effect is more significant for n = 3 stacking and p = t position. We further investigated the relation between the DA orientation and CT excitons by selecting geometries from room-temperature MD simulations in the *NVT* ensemble, starting from the stationary structures. In all cases, including n = 2, 3 stacking, p = bt, btz, or t positions, and o = f, e orientations, we considered 12 ps trajectories and took either 10 (n = 2 stacking) or 5 (n = 3 stacking) randomly chosen geometries from the last 10 ps. While the time span of the trajectories and the number of structures are admittedly insufficient to sample the thermodynamical ensemble, we consider initial conditions with different PCBM positions for each system, and long simulation times in the scale of the fast vibrational modes (stretching and bending). The procedure is hopefully adequate to indicate how robust the change in the density of low-energy CT excitons would be against temperature or fast geometry fluctuations, although keeping the computation time spent with MD simulations, excited-state calculations, and exciton analysis at a reasonable level. As shown in the Supporting Information (Figure S6), the absorption cross sections change significantly along the MD trajectories, and the oscillator strengths around 2.5, 2.7, and 2.9 eV change by 1 order of magnitude among the different snapshots. Ideally, one should perform Monte Carlo integrations to obtain reasonably converged cross sections, but this procedure would require longer MD trajectories and probably 10^3 to 10^4 geometries, which would be unfeasible.

We defined cold CT excitons based on two criteria. For each system, we considered the CT states within a 0.2 eV energy window (i) above the lowest-lying excited state with CT character and (ii) above the S_1 state. The width of the energy window is of course arbitrary, but sizeable probabilities for nonadiabatic transition are expected for energy gaps around and below 0.2 eV, which justifies the present choice. The average number of cold CT states obtained from the criterion (i,ii), respectively, denoted $\langle n_{\mathrm{CT}}^{\mathrm{cold}*} \rangle$ and $\langle n_{\mathrm{CT}}^{\mathrm{cold}} \rangle$, is shown in Table 3. The average number of CT states lying below the brightest ones, $\langle n_{\mathrm{CT}}^{\mathrm{low}} \rangle$, is also presented. In general, the different positions have a mild impact on the number of cold CT excitons, although $\langle n_{\mathrm{CT}}^{\mathrm{cold}} \rangle$, $\langle n_{\mathrm{CT}}^{\mathrm{cold}*} \rangle$, and $\langle n_{\mathrm{CT}}^{\mathrm{low}} \rangle$ tend to be smaller for p = bt and larger for p = t. The significance of these differences should be taken with caution in view of the small number of geometries considered in the averages. The impact of orientation on the number of cold CT states is much clearer than that of position, confirming the trends suggested by the spectra of the stationary structures.

The excitation spectra of the models comprising two PCBM molecules are presented in Figure 6. For the face-on orientation, we considered side-by-side arrangements in which the acceptors lie either on top of BT and BTz subunits (p = bt _btz) or on top of two T subunits (p = t _t), while for the edge-on orientation, we only considered the p = t_t case to prevent dissociation during the MD. In panel (b), we show the results for the PCBMs arranged in a row at the p = t position. In view of the weak dependence of the calculated spectra on positions, the p = bt case is shown in the Supporting Information (Figure S5), while p = btz models were not explored. It is clear from Figure 6 and Tables 2 and 3 that the 2-PCBM models share the basic features with the single-

Table 2. Lowest-Lying Absorption Bands of PTBTBTz/PCBM Models[a]

system	1st band	2nd band	3rd band
(dim-PT)$_2$(PCBM@bt)$_1$:*f*(a)	2.557 (2.245)	2.778 (1.345)	weak
(dim-PT)$_2$(PCBM@btz)$_1$:*f*(*)	2.534 (0.919)	2.802 (0.808)	weak
	2.547 (1.177)	2.806 (0.609)	
(dim-PT)$_2$(PCBM@t)$_1$:*f*(b)	2.612 (2.572)	2.775 (0.919)	weak
(dim-PT)$_2$(PCBM@bt)$_1$:*e*(c)	2.518 (0.183)	2.771 (1.266)	3.142 (0.737)
	2.587 (2.239)		
(dim-PT)$_2$(PCBM@t)$_1$:*e*(d)	2.613 (2.406)	2.709 (0.923)	3.071 (0.228)
	2.780 (0.576)		3.143 (0.561)
(dim-PT)$_3$(PCBM@bt)$_1$:*f*(e)	2.465 (1.558)	2.691 (0.591)	2.940 (0.990)
		2.696 (1.231)	2.945 (0.176)
		2.706 (0.423)	
(dim-PT)$_3$(PCBM@btz)$_1$:*f*(*)	2.460 (1.512)	2.702 (2.197)	2.934 (1.237)
			2.828 (0.215)
(dim-PT)$_3$(PCBM@t)$_1$:*f*(f)	2.428 (0.149)	2.636 (0.516)	2.937 (1.061)
	2.471 (1.319)	2.710 (2.171)	
(dim-PT)$_3$(PCBM@bt)$_1$:*e*(g)	2.464 (1.572)	2.723 (2.453)	2.969 (1.165)
			3.036 (0.130)
(dim-PT)$_3$(PCBM@t)$_1$:*e*(h)	2.490 (0.860)	2.603 (0.149)	2.914 (0.174)
		2.678 (3.244)	2.917 (0.776)
			2.931 (0.120)
(dim-PT)$_2$(PCBM@bt_btz)$_{2sd}$:*f*(i)	2.526 (2.040)	2.790 (1.110)	2.880 (0.108)
		2.804 (0.159)	2.887 (0.138)
			2.943 (0.147)
(dim-PT)$_2$(PCBM@t_t)$_{2sd}$:*f*(j)	2.531 (2.032)	2.807 (1.036)	2.941 (0.211)
		2.869 (0.269)	3.070 (0.111)
(dim-PT)$_2$(PCBM@t_t)$_{2sd}$:*e*(m)	2.632 (0.461)	2.731 (0.822)	weak
	2.636 (0.877)		
	2.652 (1.606)		
(dim-PT)$_2$(PCBM@bt)$_{2rw}$:*f*(k)	2.571 (2.236)	2.793 (1.008)	2.900 (0.129)
		2.799 (0.114)	2.955 (0.111)
			3.173 (0.592)
(dim-PT)$_2$(PCBM@t)$_{2rw}$:*f*(l)	2.569 (2.035)	2.713 (0.207)	2.900 (0.129)
	2.602 (0.185)	2.787 (1.110)	3.173 (0.600)
(dim-PT)$_2$(PCBM@bt)$_{2rw}$:*e*(n)	2.579 (2.316)	2.754 (0.235)	2.915 (0.388)
		2.794 (0.880)	2.964 (0.231)
			3.172 (0.552)
(dim-PT)$_2$(PCBM@t)$_{2rw}$:*e*(o)	2.628 (2.481)	2.723 (0.422)	2.921 (0.145)
		2.773 (0.861)	3.159 (1.081)

[a] In each case, we show the major contributions from the vertical excited states of the stationary structures, indicating the energies, in eV, and the oscillator strengths (given in parenthesis). The letter in parenthesis indicates the system in Figure 3. The two complexes with (*) are shown in Figure S3a,b of the Supporting Information.

PCBM counterparts. The spectra of CT states have significant dependence on the orientation, although not as much on the position of the acceptor molecules. The bright states mostly have an LD or MX character, despite the denser spectra of LA states. The edge-on orientation increases the density of cold CT excitons, an effect that is more evident for the p = t position than for p = bt, in the case where the PCBMs are arranged in a row (see Figure 6b and Supporting Information, Figure S5). Compared to the other models with an edge-on orientation, the 2-PCBM systems with a 2rw arrangement and an e orientation have more significant differences between $\langle n_{\text{CT}}^{\text{cold}} \rangle$ and $\langle n_{\text{CT}}^{\text{cold}*} \rangle$. The reasons for this discrepancy, which indicates cold CT excitons lying further above the S_1 states, are not clear.

4. DISCUSSION

Our analysis has shown significantly larger densities of cold CT states in edge-on than in face-on complexes. Such a density dependence on the orientation has also been previously pointed out[6,52] for other complexes with fullerene and non-fullerene acceptors. In the present work, however, we deliver a much in-depth picture of the CT exciton's dependence on the complex's architecture.

The orientation effect on the cold CT states seems to be a general property of DA interfaces[6,47,51,52,54] and can be further investigated by the fragment-based analysis outlined in Section 2. We averaged the CT numbers, defined in eq 4, for the different models using the geometries sampled from the MD simulations. We considered the cold CT states lying up to 0.2 eV above the S_1 state, such that the number of data points in each average is given by $N \times \langle n_{\text{CT}}^{\text{cold}} \rangle$, where N is the number of structures and $\langle n_{\text{CT}}^{\text{cold}} \rangle$ is the average number of cold CT states. In addition to increasing the spectral density of low-energy CT states, the edge-on orientation enhances the level of charge separation. In nearly all cases, one finds $\langle \text{CT}_{\text{cold}} \rangle < 0.9$ and $\langle \text{CT}_{\text{cold}} \rangle \geq 0.95$ for the face-on and edge-on models, respectively, regardless of the oligomer stacking as well as the number, position, and arrangement of the PCBM molecules. Although not shown here, a similar trend was found for the cold CT states defined with respect to the lowest-lying CT exciton and also for the CT states lying below the brightest states. The CT states at the bottom of the excited state spectra are believed to dissociate thermally,[5,6] a process that should be favored by the edge-on orientation given the

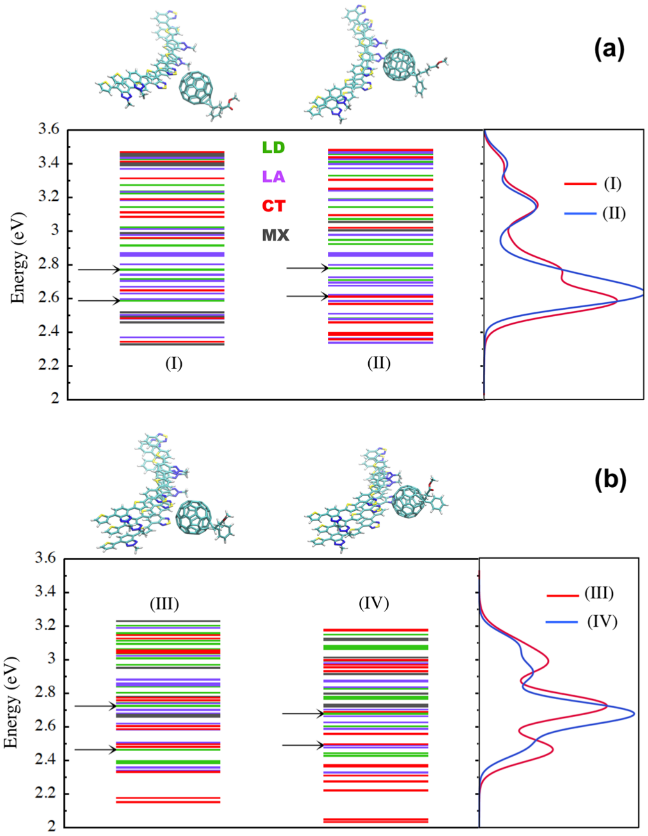

Figure 5. (a) Main panel shows the vertical excitation spectra for the (dim-PT)$_2$:(PCBM@bt)$_1$:e (I) and (dim-PT)$_2$:(PCBM@t)$_1$:e (II) systems. The LD states are indicated in green, LA in purple, CT in red, and MX in gray. The horizontal arrows point to the brightest transitions, and the geometries of the model systems are shown on top of the spectra. The right panel shows the absorption cross section (in arbitrary units) obtained from the broadening of the vertical spectra with Gaussian line shapes. (b) Same as in panel (a) for the (dim-PT)$_3$:(PCBM@bt)$_1$:e (III) and (dim-PT)$_3$:(PCBM@t)$_1$:e (IV) systems.

increased interfacial CT and the higher density of cold CT states.[6]

Further insights into the orientation effect on the CT excitons can be gained from the analysis of the POS descriptor, defined in eqs 5 and 6. The fragmentation scheme follows the conventions shown in Figures 7b and 8b for the models with n = 2, 3 stacking, respectively. For decomposition into N_{fr} fragments, the oligomer chains are labeled A = 1 to A = (N_{fr} − 1), from the furthest- to the closest-lying one with respect to the PCBM molecule, which is labeled A = N_{fr}. While the positions might not be as meaningful for the edge-on orientation, since the fragments are not aligned, the POS descriptor can still be interpreted as a weighted contribution from the fragments to the excitons. The POS descriptor for the CT states of the n = 2 stacking models is presented in Figure 7a as a function of excitation energy. We only show the data points for the stationary structures to avoid overloading the panel, but the results are representative (similar to those obtained for the other geometries considered in Table 3). The vertical shaded areas indicate the energy range of the bright states, where the brightest ones lie around ≈2.55 eV. The CT numbers, given in the color map, were obtained for two fragments, corresponding to the donor and acceptor domains, for consistency with the previous results (this procedure also avoids the fact that an LD state involving CT between the oligomer chains can be assigned as a CT exciton). From eqs 5 and 6, a CT exciton with the hole fully localized on the fragment A = 1 and the electron fully localized on the fragment A = 3 will have POS = 2.00. Accordingly, POS = 2.50 results from hole localization on the A = 2 fragment, while POS = 2.25 from an evenly delocalized hole over the A = 1, 2 fragments. These ideal cases are also indicated by the dashed lines. The cold excitons of structures with a face-on orientation essentially arise from (A = 2 → B = 3) transitions, where A and B denote, respectively, the fragments where the hole and the electron reside. The POS descriptor of those CT excitons also exceeds the limiting value of 2.50, which indicates the admixture of LA character, consistent with the relatively low CT numbers, below 0.85. Only the high-energy CT excitons, lying above 2.8 eV, display significant CT from the A = 1 fragment, although the POS descriptors for excitons with similar excitation energies spread considerably between the limits the ideal (1 → 3) and (2 → 3) transitions. These trends are consistent with TD-DFT studies on interfacial CT states of DTDCTB/C$_{60}$ models[46] with a face-on orientation. In the cold CT states, the hole mainly localizes on a single DTDCTB chain, also lying further from the electron as the energy of the CT state increases. Co-facial pentacene-C$_{60}$ systems with a face-on orientation[47] display more significant delocalization of the hole among the stacked donor chains and also larger electron−hole distances in larger models containing four pentacene molecules.

For the structures with an edge-on orientation, one finds 2.00 < POS <2.50 for both cold and hot excitons, pointing out that CT from either (or both) donor fragments can take place with no clear dependence on the photon energy. The electron−hole correlation plots for a few representative CT excitons of the (dim-PT)$_2$(PCBM@t)$_1$:f and (dim-PT)$_2$(PCBM@t)$_1$:e models are shown in Figure 7b. The convention for the hole and electron axes is defined in Figure 1c. The low-energy CT exciton of the face-on structure (2.42 eV) mostly arises from the (2 → 3) transition, while in the high-energy states, the hole resides either on the A = 1 (2.82 eV) or A = 2 (2.84 eV) donor fragments. The admixture of LA character is fairly clear for the two lowest-lying states (green shade on the A = B = 3 matrix element). The edge-on structures show low-energy CT excitons formed by transfer out of either donor fragment (2.46 and 2.57 eV) or both of them (2.36 eV). The lack of noticeable LD or LA admixture is also consistent with the more effective CT, indicated by CT > 0.95.

The POS descriptors for the stationary structures of the models with n = 3 stacking are shown in Figure 8a. While the general trends are shared with the n = 2 models, some aspects are noteworthy. Despite the more thorough CT, with CT ≈ 0.90 and a smaller admixture of LD character, the models with a face-on orientation still show cold CT excitons with holes mostly localized on the donor fragment lying the closest to the PCBM molecule. It should be clear that, according to the decomposition into four fragments, the ideal (1 → 4) and (3 → 4) transitions result in POS = 2.50 and POS = 3.50, respectively, while POS = 3.00 reflect either the ideal (2 → 4) transition, hole delocalization over non-neighboring fragments (1, 3 → 4), or uniform delocalization of the hole (1, 2, 3 → 4). Only hot CT states lying above the third absorption band have prevailing (1 → 4) character. These high-energy excitons with large electron−hole separations also show the most effective CT, with CT ≈ 1, although in general, one finds POS > 3.0

Table 3. Average Number of Cold CT Excitons Defined with Respect to the Lowest-Lying CT State, $\langle n_{\mathrm{CT}}^{\mathrm{cold}*} \rangle$, and with Respect to the S$_1$ State, $\langle n_{\mathrm{CT}}^{\mathrm{cold}} \rangle$ (see Text)[a]

system	*N*	$\langle n_{\mathrm{CT}}^{\mathrm{low}} \rangle$	$\langle n_{\mathrm{CT}}^{\mathrm{cold}*} \rangle$	$\langle n_{\mathrm{CT}}^{\mathrm{cold}} \rangle$	$\langle \mathrm{CT}_{\mathrm{cold}} \rangle$
(dim-PT)$_2$(PCBM@bt)$_1$:*f*(a)	10	(0.9 ± 0.5)	(0.8 ± 0.4)	(0.1 ± 0.3)	(0.83 ± 0.00)
(dim-PT)$_2$(PCBM@btz)$_1$:*f*(*)	10	(2.5 ± 0.7)	(1.9 ± 0.3)	(1.4 ± 0.5)	(0.87 ± 0.05)
(dim-PT)$_2$(PCBM@t)$_1$:*f*(b)	10	(2.7 ± 0.5)	(1.9 ± 0.3)	(1.7 ± 0.6)	(0.84 ± 0.03)
(dim-PT)$_2$(PCBM@all)$_1$:*f*	30	(2.0 ± 1.0)	(1.5 ± 0.6)	(1.1 ± 0.9)	(0.86 ± 0.05)
(dim-PT)$_2$(PCBM@bt)$_1$:*e*(c)	10	(4.4 ± 0.8)	(2.8 ± 0.7)	(2.2 ± 0.7)	(0.96 ± 0.05)
(dim-PT)$_2$(PCBM@t)$_1$:*e*(d)	10	(5.3 ± 0.6)	(3.7 ± 1.2)	(2.8 ± 1.6)	(0.99 ± 0.02)
(dim-PT)$_2$(PCBM@all)$_1$:*e*	20	(4.9 ± 0.9)	(3.3 ± 1.1)	(2.5 ± 1.3)	(0.97 ± 0.04)
(dim-PT)$_3$(PCBM@bt)$_1$:*f*(e)	5	(1.8 ± 1.2)	(1.4 ± 0.5)	(0.6 ± 0.5)	(0.86 ± 0.03)
(dim-PT)$_3$(PCBM@btz)$_1$:*f*(*)	5	(2.2 ± 1.2)	(1.4 ± 0.5)	(1.2 ± 0.7)	(0.93 ± 0.02)
(dim-PT)$_3$(PCBM@t)$_1$:*f*(f)	5	(1.8 ± 1.0)	(1.2 ± 0.4)	(1.2 ± 0.4)	(0.87 ± 0.06)
(dim-PT)$_3$(PCBM@all)$_1$:*f*	15	(1.9 ± 1.1)	(1.3 ± 0.5)	(1.0 ± 0.6)	(0.89 ± 0.05)
(dim-PT)$_3$(PCBM@bt)$_1$:*e*(g)	5	(6.4 ± 2.1)	(2.0 ± 0.6)	(2.0 ± 0.6)	(0.99 ± 0.01)
(dim-PT)$_3$(PCBM@t)$_1$:*e*(h)	5	(9.6 ± 1.0)	(3.2 ± 1.5)	(3.2 ± 1.5)	(0.998 ± 0.002)
(dim-PT)$_3$(PCBM@all)$_1$:*e*	10	(8.0 ± 2.2)	(2.6 ± 1.3)	(2.6 ± 1.3)	(0.995 ± 0.009)
(dim-PT)$_2$(PCBM@bt_btz)$_{2\mathrm{sd}}$:*f*(i)	5	(3.6 ± 1.7)	(1.8 ± 0.7)	(1.4 ± 0.5)	(0.88 ± 0.08)
(dim-PT)$_2$(PCBM@t_t)$_{2\mathrm{sd}}$:*f*(j)	5	(1.8 ± 1.7)	(1.4 ± 1.0)	(0.8 ± 1.2)	(0.85 ± 0.06)
(dim-PT)$_2$(PCBM@all)$_{2\mathrm{sd}}$:*f*	10	(2.7 ± 1.9)	(1.6 ± 0.9)	(1.1 ± 0.9)	(0.88 ± 0.07)
(dim-PT)$_2$(PCBM@t_t)$_{2\mathrm{sd}}$:*e*(m)	5	(10.2 ± 0.8)	(4.8 ± 1.7)	(4.0 ± 1.7)	(0.96 ± 0.03)
(dim-PT)$_2$(PCBM@bt)$_{2\mathrm{rw}}$:*f*(k)	5	(1.5 ± 1.1)	(1.3 ± 0.8)	(0.8 ± 0.8)	(0.93 ± 0.04)
(dim-PT)$_2$(PCBM@t)$_{2\mathrm{rw}}$:*f*(l)	5	(1.0 ± 0.7)	(1.0 ± 0.7)	(1.0 ± 0.7)	(0.88 ± 0.04)
(dim-PT)$_2$(PCBM@all)$_{2\mathrm{rw}}$:*f*	10	(1.3 ± 0.9)	(1.2 ± 0.7)	(0.8 ± 0.7)	(0.91 ± 0.04)
(dim-PT)$_2$(PCBM@bt)$_{2\mathrm{rw}}$:*e*(n)	5	(2.6 ± 0.5)	(2.4 ± 0.8)	(0.2 ± 0.4)	(0.89 ± 0.00)
(dim-PT)$_2$(PCBM@t)$_{2\mathrm{rw}}$:*e*(o)	5	(4.4 ± 0.5)	(2.8 ± 1.0)	(1.2 ± 1.2)	(0.98 ± 0.02)
(dim-PT)$_2$(PCBM@all)$_{2\mathrm{rw}}$:*e*	10	(3.5 ± 1.0)	(2.6 ± 0.9)	(0.7 ± 1.0)	(0.97 ± 0.04)

[a] The average number of CT states lying below the brightest state, $\langle n_{\mathrm{CT}}^{\mathrm{low}} \rangle$, and the average values of the charge-transfer number for the cold CT excitons defined with respect to S$_1$, $\langle \mathrm{CT}_{\mathrm{cold}} \rangle$, are also shown. For each system, the averages are computed for the different relative positions of the PCBM molecules (bt, btz, or t) and also without discriminating the positions (all). The number of geometries, *N*, used to calculate the n_{CT} averages and standard deviations (given in parenthesis) is indicated. The CT$_{\mathrm{cold}}$ values are averaged over the CT states, not over the geometries. The letter in parenthesis indicates the system in Figure 3. The two interfaces with (*) are shown in Figure S3a,b of the Supporting Information.

and CT ≈ 0.9 for the face-on models. The electron−hole correlation plots for representative CT excitons of the (dim-PT)$_3$:(PCBM@t)$_1$:*f* structure are shown in Figure 8b. In contrast, the edge-on orientation mostly gives rise to POS ≈ 3, suggesting more effective hole delocalization over the donor chains, according to the ideal transitions described above. Only for high-energy CT excitons, around and above the third band, the values of the POSs are more spread. In general, the CT is more effective, as previously pointed out, and the hole delocalization is also clear from the correlation plots of the representative CT excitons, as shown in Figure 8b.

The POS descriptor is expected to correlate with the exciton size (d_{exc}, see eqs 7 and 8), which would significantly impact the dissociation of cold interfacial excitons.[50] The connection between the exciton size and the average positions of the hole and electron (POS, see eq 6) might be affected by several aspects, such as the degree of (de)localization of the particles within a given fragment, the fragmentation scheme employed to define the POS descriptors, and the detailed structure of the 1-TDM. The approximations underlying eq 8, particularly the definition of atomic volumes with constant electron−hole distances for the atomic pairs, might also impact the results. While we did not explore more complex fragmentation schemes to investigate the quasi-particle delocalization in detail, d_{exc} is shown in Figure 9a for the CT states of the models with $n = 3$ stacking (stationary structures). The exciton size is plotted against the POS descriptor obtained from four fragments as before and also the two-fragment CT number, indicated by the color map. Different positions are not discriminated, so we focus on the orientations. The face-on models (circles) display a stronger d_{exc} dependence on position since the (de)localization of the hole over different donor chains has a clear effect on the charge separation, with the electron essentially localized on the PCBM molecule. In case the hole is localized on the $A = 3$ fragment, which is the oligomer chain lying the closest to the acceptor (POS ≈ 3.5), we obtain $d_{\mathrm{exc}} \approx 9.5$ Å. For the CT states with POS ≈ 2.5, consistent with (1 → 4) transitions, one finds $d_{\mathrm{exc}} \approx 14.5$ Å. As discussed above, the localization of the hole on the $A = 3$ and $A = 1$ fragments typically produces low- and high-energy CT excitons, respectively. A few ideal excitations might be of help to better understand the intermediate values of the POS descriptor. The even delocalization of the hole over two fragments leads to (1, 2 → 4) and (2, 3 → 4) transitions and hence to POS = 2.75 and POS = 3.25, respectively. As mentioned above, POS = 3.00 can arise from either (2 → 4), (1, 3 → 4), or (1, 2, 3 → 4) ideal excitations. Most of the excited states have POS > 3.00, with the degree of CT generally increasing with the exciton size. As a rule of thumb, face-on models give rise to CT excitons that increase in size and charge separation as a function of the excitation energy, according to the results shown in Figures 8a and 9a.

The edge-on models (triangles) do not show a clear relation between position and excitation energy, as discussed above. The d_{exc} dependence on position is not evident, either, since nearly all points lie within (2.75 < POS <3.25). This suggests hole delocalization over the donor chains, although with no clear trend, since several ideal transitions have POS descriptors

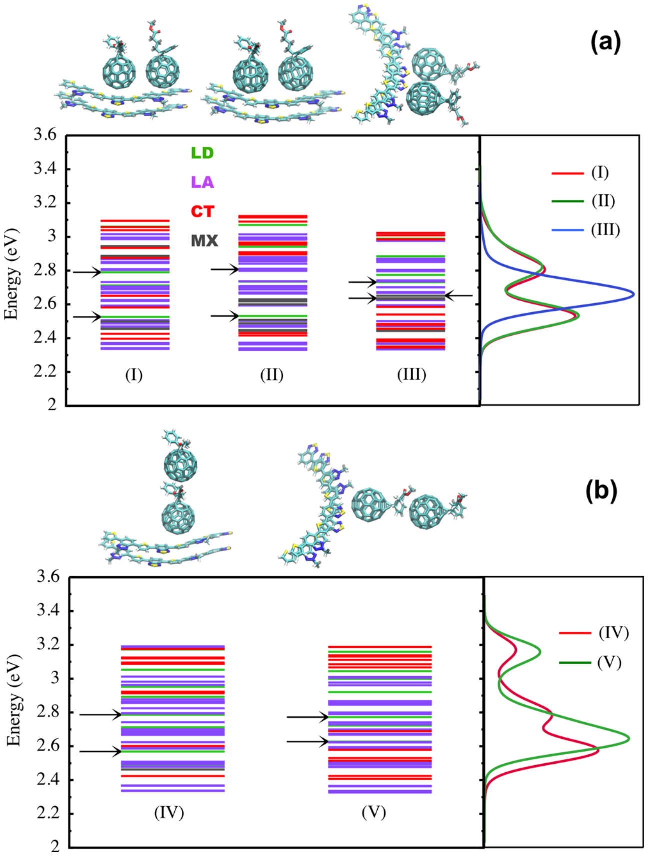

Figure 6. (a) Main panel shows the vertical excitation spectra for the (dim-PT)$_2$:(PCBM@bt_btz)$_{2sd}$:*f* (I), (dim-PT)$_2$:(PCBM@t_t)$_{2sd}$:*f* (II), and (dim-PT)$_2$:(PCBM@t_t)$_{2sd}$:*e* (III) systems. The LD states are indicated in green, LA in purple, CT in red, and MX in gray. The horizontal arrows point to the brightest transitions, and the geometries of the model systems are shown on top of the spectra. The right panel shows the absorption cross section (in arbitrary units) obtained from the broadening of the vertical spectra with Gaussian line shapes. (b) Same as in panel (a) for the (dim-PT)$_2$:(PCBM@t)$_{2rw}$:*f* (IV) and (dim-PT)$_2$:(PCBM@t)$_{2rw}$:*e* (V) systems.

lying in that range. Also as a rule of thumb, the exciton size increases with the degree of CT and the excitation energy, as inferred from Figures 8a and 9a. Inspection of the electron−hole correlation plots (not shown) indicates that the largest excitons arise from excitations having either dominant (1, 3 → 4) or (1, 2, 3 → 4) characters. While it makes physical sense that these transitions produce large excitons, as they maximize the delocalization of the hole, the present analysis provides limited information since smaller CT excitons have similar fragment contributions. Breaking the complexes into more fragments could provide more detailed information, but we do not pursue this goal in the present work. In any case, exciton sizes as large as $d_{exc} \approx 15$ Å are found for both orientations, although the electron−hole characteristics are not the same. Apart from the delocalization along the chains, the face-on models produce larger excitons by placing the hole on oligomer chains lying far from the acceptor, whereas larger excitons are produced by the delocalization of the hole in edge-on models.

The delocalization of the hole along the oligomer chains was further explored with models composed of PTBTBTz tetramers, namely, (tet-PT)$_2$(PCBM@*p*)$_1$:*f*, and also PT3BTBTz dimers, (dim-PT3)$_2$(PCBM@*p*)$_1$:*f*. The data in

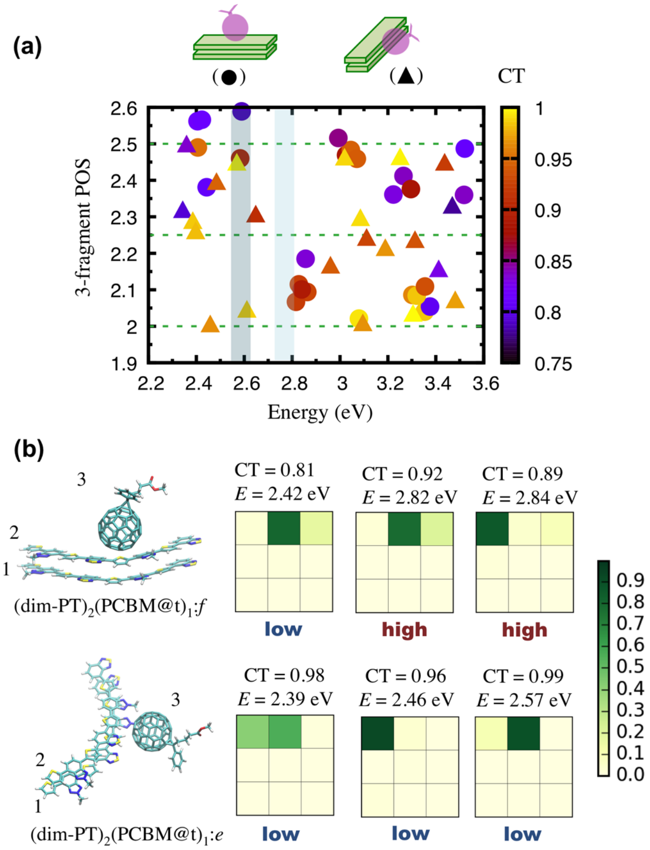

Figure 7. (a) Position (POS) descriptor for the CT states as a function of excitation energy. The color map indicates the corresponding CT numbers. The data points were obtained for the stationary structures of complexes with *n* = 2 stacked chains in the donor domain (dim-PT)$_2$:(PCBM@*p*)$_1$:*f* (circles) with *p* = bt, btz, or t and (dim-PT)$_2$:(PCBM@*p*)$_1$:*e* (triangles) with *p* = bt or t. The POS numbers were computed for the three-fragment decomposition shown on the left-hand side of the panel (b), although the CT numbers were obtained from a two-fragment (DA) decomposition scheme. The horizontal dashed lines correspond to the POS values of ideal CT states with the hole localized on fragment 1 (POS = 2.00), localized on fragment 2 (POS = 2.50), or evenly delocalized over fragments 1 and 2 (POS = 2.25). The shaded regions indicate the energy range where the bright states are found (the brightest states of the five structures lie at ≈2.55 eV). (b) Structures of the (dim-PT)$_2$:(PCBM@t)$_1$:*o* models, with *o* = *f*, *e* orientations, are shown on the left-hand side along with the fragmentation convention. Electron−hole correlation plots for selected CT states are presented on the right-hand side, following the convention given in Figure 1c. The CT states are indicated as "high" and "low" in case they lie above or below the brightest state.

Figure 9b, obtained for stationary structures, spread considerably, such that exciton sizes around and below 14 Å are found for the face-on models built on (dim-PT)$_2$, (tet-PT)$_2$, and (dim-PT3)$_2$ donors. Nevertheless, larger excitons are produced using the two larger models, as expected, and the trend of size increase with the CT number is once more noticeable. Despite the limited number of data points, the largest excitons (15 Å < d_{ext} < 18 Å) are mostly built on PT3BTBTz dimers. In general, the (dim-PT3)$_2$ donors remain more planar during MD and geometry optimization than the (tet-PT)$_2$ counterparts (see the structures in Supporting Information, Figures S2 and S3), which favors the delocalization of the molecular orbitals and hence the delocalization of

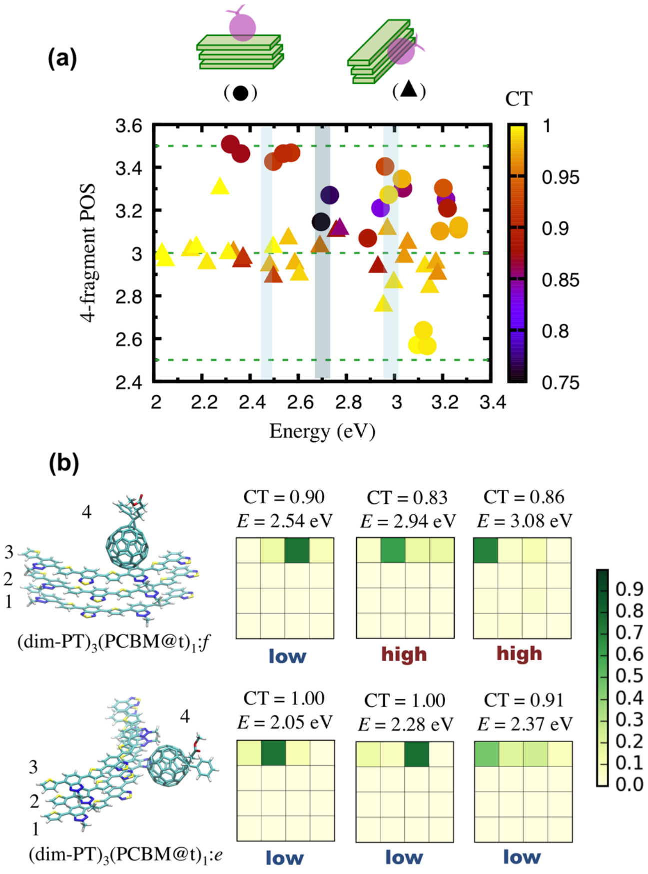

Figure 8. (a) Position (POS) descriptor for the CT states as a function of excitation energy. The color map indicates the corresponding CT numbers. The data points were obtained for the stationary structures of the complexes with $n = 3$ stacked chains in the donor domain (dim-PT)$_3$:(PCBM@p)$_1$:f (circles) with p = bt, btz, or t and (dim-PT)$_3$:(PCBM@p)$_1$:e (triangles) with p = bt or t. The POS numbers were computed for the four-fragment decomposition shown on the left-hand side of panel (b), although the CT numbers were obtained from a two-fragment (DA) decomposition scheme. The horizontal dashed lines correspond to the POS values of ideal CT states with the hole localized on fragment 1 (POS = 2.5), localized on fragment 3 (POS = 3.5), and either localized on fragment 2 or evenly delocalized over fragments 1, 2, and 3 (POS = 3.0). The shaded regions indicate the energy range where the bright states are found (the brightest states of the five structures lie at ≈2.7 eV). (b) Structures of the (dim-PT)$_3$:(PCBM@t)$_1$:o models, with o = f, e orientations, are shown on the left-hand side along with the fragmentation convention. Electron−hole correlation plots for selected CT states are presented on the right-hand side, following the convention given in Figure 1c. The CT states are indicated as "high" and "low" in case they lie above or below the brightest state.

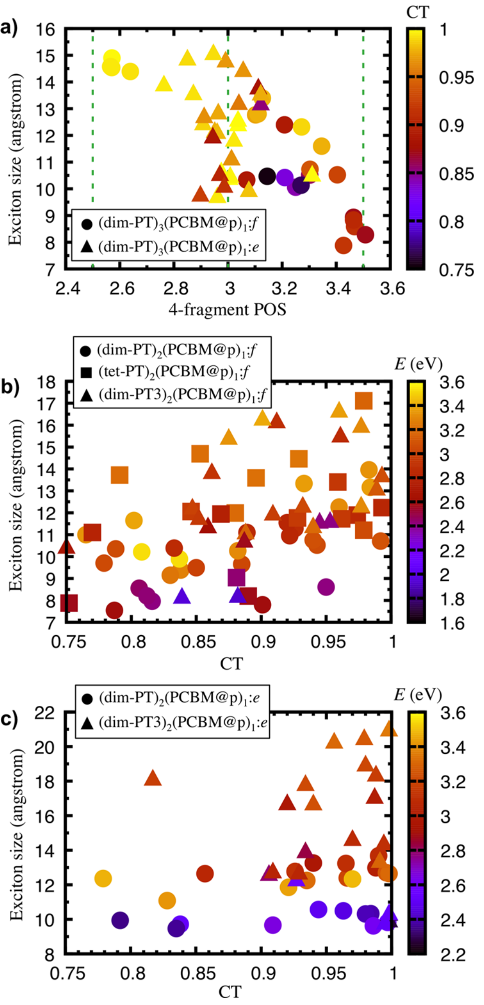

Figure 9. (a) Exciton size against the POS and the CT number, given in the color map, for the systems indicated in the panel. In each case, we consider different positions of the PCBM molecule: p = bt, btz, or t (circles); p = bt or t (triangles). The vertical lines indicate the POS descriptor values for ideal excitations (see Figure 8a). (b) Exciton size against the CT number and the excitation energy, given in the color map, for the face-on models indicated in the panel. The PCBM positions are p = bt or btz (circles); p = bt or t (squares); and p = bt, btz, or t (triangles) (c) Same as in panel (b), for the edge-on models with positions p = bt or t (circles and triangles).

the hole. The exciton sizes for the edge-on models built on (dim-PT)$_2$ and (dim-PT3)$_2$ donors are presented in Figure 9c. The latter donors produce larger excitons with more thorough charge separation. We mention in passing that the PT3BTBTz/PCBM OSCs are more efficient than the PTBTBTz/PCBM ones. While we cannot draw conclusions on the efficiencies of the devices from the present models, the atomistic simulations point out two aspects that could contribute to the higher efficiency of the PT3BTBTz/PCBM cells, namely, the stiffer donor chains that favor exciton delocalization and larger oscillator strengths (between ≈4 and ≈6 for the brightest bands). Finally, the edge-on PT3BTBTz models produce considerably larger excitons, 18 Å < d_{exc} < 22 Å, than the face-on counterparts. This is in contrast with the (dim-PT)$_3$ models, with similar exciton sizes for both orientations. One must notice, however, that the n = 2 stacking poses a limit for electron−hole separation in the face-on (dim-PT3)$_2$ donors, preventing the formation of larger excitons.

We now turn our attention to the delocalization of the electron, exploring the complexes with two PCBM molecules. The exciton sizes of the CT states are shown in Figure 10 for the systems with the acceptor units arranged side-by-side. For the face-on orientation (circles), the CT excitons lying around and below the second absorption band ($\lesssim$2.8 eV) have small sizes, d_{exc} < 9.0 Å, since they are essentially given by (2 → 3) and (2 → 4) transitions, according to the fragment labels indicated in the top panel. The values of the POS descriptor spread considerably because the charge can be transferred to either of the PCBM molecules (A = 3 or A = 4). In our

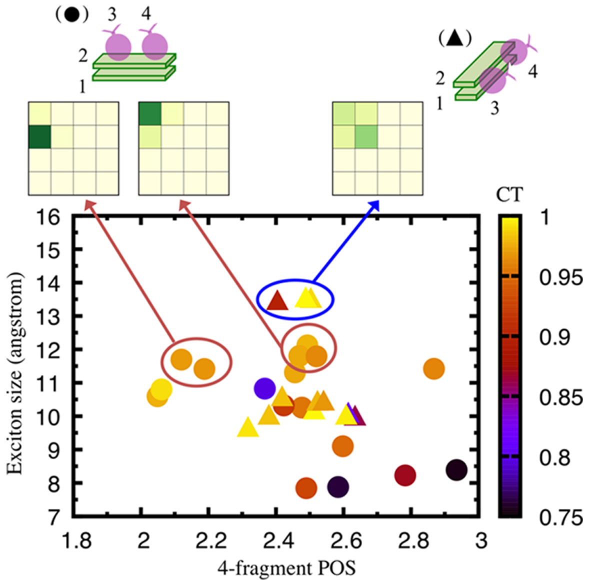

Figure 10. Exciton size against the POS and the CT number, given in the color map, for the systems (dim-PT)$_2$(PCBM@p)$_{2sd}$:f (circles) and (dim-PT)$_2$(PCBM@p)$_{2sd}$:e (triangles). In both cases, the data points include the p = bt_btz, t_t positions. Representative electron−hole correlation plots are shown above the main panel, with the fragment labels (1−4) indicated on the top.

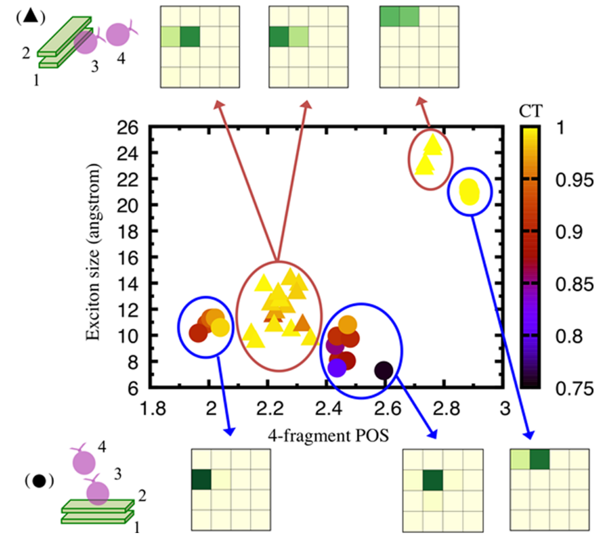

Figure 11. Exciton size against the POS and the CT number, given in the color map, for the systems (dim-PT)$_2$(PCBM@p)$_{2rw}$:f (circles) and (dim-PT)$_2$(PCBM@p)$_{2rw}$:e (triangles). In both cases, the data points include the p = bt or t positions. Representative electron−hole correlation plots are shown above and below the main panel, with the fragment labels (1−4) indicated on the left.

calculations, the electron did not delocalize over the two acceptor units, even for the higher-energy CT states, such that the largest exciton sizes, d_{exc} ≈ 12 Å, mostly correspond to (1 → 3) and (1 → 4) transitions, as indicated by the selected correlation plots in Figure 10. The two PCBM molecules arranged side-by-side do not give rise to larger excitons compared to the analogous models, built on (dim-PT)$_2$ donors, with a single PCBM molecule (see Figure 9b). This result is consistent with TD-DFT computations for pentacene/C$_{60}$ models.[36] Only the larger systems, comprising three C$_{60}$ units, have low-energy CT states with electron delocalization over the acceptor molecules. The negative charge remains localized on a single C$_{60}$ for smaller models with up to two molecules in the acceptor domain.

In the case of edge-on orientation (triangles), we mostly obtained delocalized holes for the lower-lying CT excitons produced by (1, 2 → 3) or (1, 2 → 4) transitions, while both the hole and the electron tend to delocalize for the higher-energy CT states. The fully delocalized high-energy CT states are illustrated by the correlation plot in Figure 10, having d_{exc} ≈ 13.5 Å. As for the face-on orientation, the addition of a PCBM molecule does not significantly alter the sizes of the largest excitons compared to the similar edge-on models with a single PCBM molecule (not shown). This happens because the delocalization of the electron is compensated by the smaller electron−hole distances.

For the models with two PCBM molecules arranged in a row, the dependence of the CT exciton sizes with respect to the POS descriptor and CT number is presented in Figure 11, along with electron−hole correlation plots for representative states. Once more, we do not distinguish the positions and concentrate on the orientations. The CT states of the face-on systems (circles) fall into three distinct regions. The low-energy excitons are typically formed by (2 → 3) transitions, where the donor fragments are labeled 1 and 2, while the acceptor fragments, 3 and 4, as indicated in the panel. Ideally, those transitions are characterized by POS = 2.5. The CT excitons with POS = 2.0 are mostly formed out of (1 → 3) transitions, having intermediate energies, while only at the higher energies we observe significant electron delocalization on the A = 4 fragment, corresponding to the PCBM molecule lying further from the donor domain. In the latter case, the exciton sizes significantly increase to d_{exc} ≈ 21 Å. Although the data points are somewhat scattered, the edge-on models produce larger low-energy excitons than the face-on counterparts, as they allow for the delocalization of the hole over the oligomer chains. Only for the high-energy CT excitons, however, the electron delocalizes over the far-lying PCBM molecule. This combination of a delocalized hole (over the two stacked chains) and a distant electron produces the largest CT states among all the models explored in the present study, with d_{exc} ≈ 24 Å.

The delocalization of the interfacial CT excitons is, of course, limited by the system sizes, but some of the trends are compatible with those obtained from tight-binding models for much larger interfaces.[6] In the latter models, the higher-energy CT states have a band-like structure, approaching charge-separated states. On average, the electron−hole distances are smaller for the model in which the hole tends to delocalize along the DA interface. This result is in line with the present ones for the models having two PCBM molecules arranged side-by-side since the high-energy exciton sizes are not particularly large even when delocalized over all fragments. In case the acceptor molecules are arranged in a row, the delocalization of the high-energy CT excitons is more perpendicular to the interface, producing larger electron−hole distances. From the photophysics perspective, the present study points out to similar trends as the previous TD-DFT study on P3HT/PCBM models.[52] Hot CT states, having energies around the absorption bands, would be expected to play a more significant part in phases with a face-on orientation. Cold CT excitons, lying close to the S$_1$ state, would be more relevant to those with an edge-on orientation.

Population transfer to cold excitons is favored by the higher density of those states and also by the cascade of CT excitons lying below the brightest states (see Figures 5 and 6). Once hot CT excitons are populated from the bright states, relaxation to lower CT states would require smaller electronic rearrangement, compared to LD and LA states, such that stronger diabatic couplings could be expected. Finally, the role of entropic forces arising from the density of electronic states in the dissociation of hot CT excitons has been recently pointed out,[6] but we cannot explore those entropy effects based on the present models.

5. CONCLUSIONS

We have employed the TD-LC-DFTB method and fragment-based 1-TDM analysis to study the CT states of polymer/fullerene interfaces, exploring models of different sizes, as well as different positions and orientations of the acceptor molecules with respect to those of the donor domain. The orientation effect is significant since the edge-on models have denser spectra of cold CT excitons, lying below the absorption bands. This effect was observed for all models addressed in the present study, taking into consideration both the stationary structures and the geometries obtained from MD simulations. The interface orientation is thus expected to have an impact on the excited-state dynamics and charge-separation mechanisms.

Phases with a face-on orientation favor dissociation from hot excitons, lying around the brightest bands. Edge-on phases favor dissociation following relaxation to cold CT states, which is enhanced by the cascade of CT excitons. These photophysical mechanisms, summarized in Figure 12, are consistent with previous atomistic simulations.[52] The exciton analysis also points out to the formation of low-energy interfacial CT states with increased electron−hole separation in the edge-on phases. This effect would also make the charge separation from cold CT states more efficient, along with the higher density of these low-energy states.

The position of the acceptor molecules with respect to the donor is generally less important, although the change in the excitation spectra from the face-on to the edge-on orientation tends to be more clear when the PCBM molecule lies closer to the T subunit of the donor chains. The face-on orientation gives rise to fewer cold CT states, which also have, on average, smaller CT numbers compared to the cold CT states in the models with the edge-on orientation. The degree of CT and the CT exciton size tend to increase with the excitation energy. In the edge-on models with a single PCBM molecule, the CT is favored by longer electron−hole distances arising from hole localization on donor chains lying far from the acceptor molecules, while hole delocalization over different donor chains prevails in the edge-on interfaces. The models with two acceptor molecules suggest that the electron remains localized on a single molecule in the cold CT states. The delocalization over two PCBM molecules was observed for higher energy CT states, although the impact on the exciton size also depends on the orientation. Larger excitons are produced by the delocalization of the electron perpendicularly to the DA interface. In case the delocalization is parallel to the interface, it is compensated by the smaller electron−hole distances, producing moderately sized CT excitons.

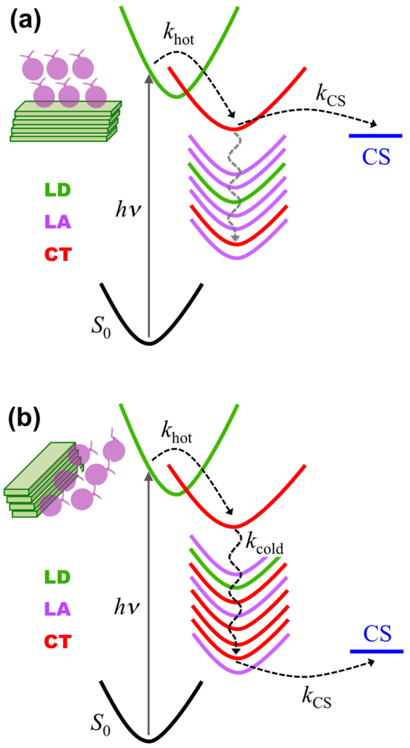

Figure 12. Mechanisms for charge separation. (a) Face-on orientation. Photoexcitation to an LD bright state is followed by nonadiabatic population transfer to a hot CT state (rate constant k_{hot}). Decay to the cold CT states (gray wavy line) is not likely to take place, so charge separation mostly proceeds from the hot CT exciton (rate constant k_{CS}). (b) Edge-on orientation. Relaxation from the hot CT exciton to the cold CT excitons (rate constant k_{cold}) is favored by the high density of low-energy CT states. Charge separation mostly proceeds from the cold CT excitons at the bottom of the excitation band.

■ ASSOCIATED CONTENT

Supporting Information

The Supporting Information is available free of charge at https://pubs.acs.org/doi/10.1021/acs.jpcc.0c10762.

Details of the MD simulations and geometry optimization; structures of the PTBTBTz stacked dimer, the PT3BTBtz monomer, and the DA complexes not shown in the main text; photoabsorption cross sections for the PTBTBTz monomer calculated by the nuclear ensemble method; vertical excitation spectra of the (dim-PT)$_2$:(PCBM@bt)$_{2rw}$:*f* and (dim-PT)$_2$:(PCBM@bt)$_{2rw}$:*e* models; photoabsorption cross sections for geometries randomly chosen from the MD simulations for the (dim-PT)$_2$(PCBM@t)$_1$:*f*, (dim-PT)$_2$(PCBM@t)$_1$:*e*, (dim-PT)$_3$(PCBM@t)$_1$:*f*, and (dim-PT)$_3$(PCBM@t)$_1$:*e* models; Cartesian coordinates of the DA complexes (PDF)

Re-parametrized OB2 Slater−Koster parameters (ZIP)

■ AUTHOR INFORMATION

Corresponding Author

Márcio T. do N. Varella − *Instituto de Física, Universidade de São Paulo, São Paulo, São Paulo 05508-090, Brazil;* orcid.org/0000-0002-5812-0342; Email: mvarella@if.usp.br

Authors

Ljiljana Stojanović − *School of Biological and Chemical Sciences, Queen Mary University of London, London E1 4NS, U.K.;* orcid.org/0000-0003-2821-5110

Van Quan Vuong − *Bredesen Center for Interdisciplinary Research and Graduate Education, University of Tennessee, Knoxville, Tennessee 37996, United States*

Stephan Irle − *Bredesen Center for Interdisciplinary Research and Graduate Education, University of Tennessee, Knoxville, Tennessee 37996, United States; Computational Sciences and Engineering Division, Oak Ridge National Laboratory, Oak Ridge, Tennessee 37831, United States;* orcid.org/0000-0003-4995-4991

Thomas A. Niehaus − *Univ Lyon, Université Claude Bernard Lyon 1, CNRS, Institut Lumière Matière, 69622 Villeurbanne CEDEX, France;* orcid.org/0000-0001-9576-7658

Mario Barbatti − *Aix Marseille University, CNRS, ICR, Marseille, France;* orcid.org/0000-0001-9336-6607

Complete contact information is available at:
https://pubs.acs.org/10.1021/acs.jpcc.0c10762

Notes

The authors declare no competing financial interest.

■ ACKNOWLEDGMENTS

M.T.d.N.V. acknowledges support from FAPESP (grant 2018/22948-0) and also from the Brazilian National Council for Scientific and Technological Development (CNPq), grant 304571/2018-0. The calculations were partly performed with HPC resources from STI (University of São Paulo), Centro Nacional de Processamento de Alto Desempenho em São Paulo (CENAPAD-SP), and the Mesocentre at the Aix Marseille University (project Equip@Meso, ANR-10-EQPX-29-01). V.Q.V. acknowledges support by an Energy Science and Engineering Fellowship of the Bredesen Center for Interdisciplinary Research and Graduate Education at the University of Tennessee, Knoxville. S.I. acknowledges support by the Laboratory Directed Research and Development (LDRD) Program of Oak Ridge National Laboratory. ORNL is managed by UT-Battelle, LLC, for DOE under contract DE-AC05-00OR22725. T.N. would like to thank the Laboratoire d'excellence iMUST for financial support. M. B. thanks the support of the Excellence Initiative of the Aix Marseille University (A*MIDEX). This manuscript has been authored by UT-Battelle, LLC, under Contract no. DE-AC05-00OR22725 with the U.S. Department of Energy. The United States Government retains and the publisher, by accepting the article for publication, acknowledges that the United States Government retains a nonexclusive, paid-up, irrevocable, worldwide license to publish or reproduce the published form of this manuscript, or allow others to do so, for United States Government purposes. The Department of Energy will provide public access to these results of federally sponsored research in accordance with the DOE Public Access Plan (http://energy.gov/downloads/doe-public-access-plan).

■ REFERENCES

(1) Clarke, T. M.; Durrant, J. R. Charge photogeneration in organic solar cells. *Chem. Rev.* **2010**, *110*, 6736−6767.

(2) Benduhn, J.; Tvingstedt, K.; Piersimoni, F.; Ullbrich, S.; Fan, Y.; Tropiano, M.; McGarry, K. A.; Zeika, O.; Riede, M. K.; Douglas, C. J.; et al. Intrinsic non-radiative voltage losses in fullerene-based organic solar cells. *Nat. Energy* **2017**, *2*, 17053.

(3) Vandewal, K. Interfacial charge transfer states in condensed phase systems. *Annu. Rev. Phys. Chem.* **2016**, *67*, 113−133.

(4) Coropceanu, V.; Chen, X.-K.; Wang, T.; Zheng, Z.; Brédas, J.-L. Charge-transfer electronic states in organic solar cells. *Nat. Rev. Mater.* **2019**, *4*, 689−707.

(5) Dimitrov, S. D.; Azzouzi, M.; Wu, J.; Yao, J.; Dong, Y.; Tuladhar, P. S.; Schroeder, B. C.; Bittner, E. R.; McCulloch, I.; Nelson, J.; et al. Spectroscopic investigation of the effect of microstructure and energetic offset on the nature of interfacial charge transfer states in polymer: fullerene blends. *J. Am. Chem. Soc.* **2019**, *141*, 4634−4643.

(6) Kafle, T. R.; Kattel, B.; Wanigasekara, S.; Wang, T.; Chan, W. L. Spontaneous Exciton Dissociation at Organic Semiconductor Interfaces Facilitated by the Orientation of the Delocalized Electron-Hole Wavefunction. *Adv. Energy Mater.* **2020**, *10*, 1904013.

(7) Tanguy, L.; Fleury, A.; Karsenti, P.-L.; Brisard, G.; Soldera, A.; Harvey, P. D. Ultrafast Energy Transfer from Local Exciton to Intermolecular CT States in a Supramolecular Model of the Donor-Acceptor Interfaces. *J. Phys. Chem. C* **2020**, *124*, 16248−16260.

(8) Zhao, W.; Li, S.; Yao, H.; Zhang, S.; Zhang, Y.; Yang, B.; Hou, J. Molecular optimization enables over 13% efficiency in organic solar cells. *J. Am. Chem. Soc.* **2017**, *139*, 7148−7151.

(9) Meng, L.; Zhang, Y.; Wan, X.; Li, C.; Zhang, X.; Wang, Y.; Ke, X.; Xiao, Z.; Ding, L.; Xia, R.; et al. Organic and solution-processed tandem solar cells with 17.3% efficiency. *Science* **2018**, *361*, 1094−1098.

(10) Yuan, J.; Zhang, Y.; Zhou, L.; Zhang, G.; Yip, H.-L.; Lau, T.-K.; Lu, X.; Zhu, C.; Peng, H.; Johnson, P. A.; et al. Single-junction organic solar cell with over 15% efficiency using fused-ring acceptor with electron-deficient core. *Joule* **2019**, *3*, 1140−1151.

(11) Cui, Y.; Yao, H.; Zhang, J.; Zhang, T.; Wang, Y.; Hong, L.; Xian, K.; Xu, B.; Zhang, S.; Peng, J.; et al. Over 16% efficiency organic photovoltaic cells enabled by a chlorinated acceptor with increased open-circuit voltages. *Nat. Commun.* **2019**, *10*, 2515.

(12) Jailaubekov, A. E.; Willard, A. P.; Tritsch, J. R.; Chan, W.-L.; Sai, N.; Gearba, R.; Kaake, L. G.; Williams, K. J.; Leung, K.; Rossky, P. J.; et al. Hot charge-transfer excitons set the time limit for charge separation at donor/acceptor interfaces in organic photovoltaics. *Nat. Mater.* **2013**, *12*, 66−73.

(13) Grancini, G.; Maiuri, M.; Fazzi, D.; Petrozza, A.; Egelhaaf, H.-J.; Brida, D.; Cerullo, G.; Lanzani, G. Hot exciton dissociation in polymer solar cells. *Nat. Mater.* **2013**, *12*, 29−33.

(14) Savoie, B. M.; Rao, A.; Bakulin, A. A.; Gelinas, S.; Movaghar, B.; Friend, R. H.; Marks, T. J.; Ratner, M. A. Unequal partnership: asymmetric roles of polymeric donor and fullerene acceptor in generating free charge. *J. Am. Chem. Soc.* **2014**, *136*, 2876−2884.

(15) van der Hofstad, T. G. J.; Di Nuzzo, D.; van den Berg, M.; Janssen, R. A. J.; Meskers, S. C. J. Influence of Photon Excess Energy on Charge Carrier Dynamics in a Polymer-Fullerene Solar Cell. *Adv. Energy Mater.* **2012**, *2*, 1095−1099.

(16) Vandewal, K.; Albrecht, S.; Hoke, E. T.; Graham, K. R.; Widmer, J.; Douglas, J. D.; Schubert, M.; Mateker, W. R.; Bloking, J. T.; Burkhard, G. F.; et al. Efficient charge generation by relaxed charge-transfer states at organic interfaces. *Nat. Mater.* **2014**, *13*, 63−68.

(17) Gregg, B. A. Entropy of charge separation in organic photovoltaic cells: the benefit of higher dimensionality. *J. Phys. Chem. Lett.* **2011**, *2*, 3013−3015.

(18) Monahan, N. R.; Williams, K. W.; Kumar, B.; Nuckolls, C.; Zhu, X.-Y. Direct observation of entropy-driven electron-hole pair separation at an organic semiconductor interface. *Phys. Rev. Lett.* **2015**, *114*, 247003.

(19) Yao, Y.; Xie, X.; Ma, H. Ultrafast Long-Range Charge Separation in Organic Photovoltaics: Promotion by Off-Diagonal Vibronic Couplings and Entropy Increase. *J. Phys. Chem. Lett.* **2016**, *7*, 4830−4835.

(20) Sánchez-Carrera, R. S.; Paramonov, P.; Day, G. M.; Coropceanu, V.; Brédas, J.-L. Interaction of charge carriers with

lattice vibrations in oligoacene crystals from naphthalene to pentacene. *J. Am. Chem. Soc.* **2010**, *132*, 14437−14446.

(21) Falke, SM; Rozzi, CA; Brida, D.; Maiuri, M.; Amato, M.; Sommer, E.; De Sio, A.; Rubio, A.; Cerullo, G.; Molinari, E.; et al. Coherent ultrafast charge transfer in an organic photovoltaic blend. *Science* **2014**, *344*, 1001−1005.

(22) Chen, X.-K.; Coropceanu, V.; Brédas, J.-L. Assessing the nature of the charge-transfer electronic states in organic solar cells. *Nat. Commun.* **2018**, *9*, 5295.

(23) Coffey, D. C.; Larson, B. W.; Hains, A. W.; Whitaker, J. B.; Kopidakis, N.; Boltalina, O. V.; Strauss, S. H.; Rumbles, G. An optimal driving force for converting excitons into free carriers in excitonic solar cells. *J. Phys. Chem. C* **2012**, *116*, 8916−8923.

(24) Dimitrov, S. D.; Bakulin, A. A.; Nielsen, C. B.; Schroeder, B. C.; Du, J.; Bronstein, H.; McCulloch, I.; Friend, R. H.; Durrant, J. R. On the energetic dependence of charge separation in low-band-gap polymer/fullerene blends. *J. Am. Chem. Soc.* **2012**, *134*, 18189−18192.

(25) Bakulin, A. A.; Dimitrov, S. D.; Rao, A.; Chow, P. C.; Nielsen, C. B.; Schroeder, B. C.; McCulloch, I.; Bakker, H. J.; Durrant, J. R.; Friend, R. H. Charge-transfer state dynamics following hole and electron transfer in organic photovoltaic devices. *J. Phys. Chem. Lett.* **2013**, *4*, 209−215.

(26) Kawashima, K.; Tamai, Y.; Ohkita, H.; Osaka, I.; Takimiya, K. High-efficiency polymer solar cells with small photon energy loss. *Nat. Commun.* **2015**, *6*, 10085.

(27) Liu, J.; Chen, S.; Qian, D.; Gautam, B.; Yang, G.; Zhao, J.; Bergqvist, J.; Zhang, F.; Ma, W.; Ade, H.; et al. Fast charge separation in a non-fullerene organic solar cell with a small driving force. *Nat. Energy* **2016**, *1*, 16089.

(28) Cheng, P.; Li, G.; Zhan, X.; Yang, Y. Next-generation organic photovoltaics based on non-fullerene acceptors. *Nat. Photonics* **2018**, *12*, 131−142.

(29) Chen, S.; Wang, Y.; Zhang, L.; Zhao, J.; Chen, Y.; Zhu, D.; Yao, H.; Zhang, G.; Ma, W.; Friend, R. H.; et al. Efficient nonfullerene organic solar cells with small driving forces for both hole and electron transfer. *Adv. Mater.* **2018**, *30*, 1804215.

(30) Qian, D.; Zheng, Z.; Yao, H.; Tress, W.; Hopper, T. R.; Chen, S.; Li, S.; Liu, J.; Chen, S.; Zhang, J.; et al. Design rules for minimizing voltage losses in high-efficiency organic solar cells. *Nat. Mater.* **2018**, *17*, 703−709.

(31) Saito, T.; Natsuda, S.-i.; Imakita, K.; Tamai, Y.; Ohkita, H. Role of Energy Offset in Nonradiative Voltage Loss in Organic Solar Cells. *Sol. RRL* **2020**, *4*, 2000255.

(32) Tummala, N. R.; Zheng, Z.; Aziz, S. G.; Coropceanu, V.; Brédas, J.-L. Static and dynamic energetic disorders in the C60, PC61BM, C70, and PC71BM fullerenes. *J. Phys. Chem. Lett.* **2015**, *6*, 3657−3662.

(33) Tummala, N. R.; Elroby, S. A.; Aziz, S. G.; Risko, C.; Coropceanu, V.; Brédas, J.-L. Packing and Disorder in Substituted Fullerenes. *J. Phys. Chem. C* **2016**, *120*, 17242−17250.

(34) Zheng, Z.; Tummala, N. R.; Fu, Y.-T.; Coropceanu, V.; Brédas, J.-L. Charge-Transfer States in Organic Solar Cells: Understanding the Impact of Polarization, Delocalization, and Disorder. *ACS Appl. Mater. Interfaces* **2017**, *9*, 18095−18102.

(35) Shi, L.; Lee, C. K.; Willard, A. P. The enhancement of interfacial exciton dissociation by energetic disorder is a non-equilibrium effect. *ACS Cent. Sci.* **2017**, *3*, 1262−1270.

(36) Zheng, Z.; Tummala, N. R.; Wang, T.; Coropceanu, V.; Brédas, J.-L. Charge-Transfer States at Organic−Organic Interfaces: Impact of Static and Dynamic Disorders. *Adv. Energy Mater.* **2019**, *9*, 1803926.

(37) Jiang, H.; Hu, P.; Ye, J.; Zhang, K. K.; Long, Y.; Hu, W.; Kloc, C. Tuning of the degree of charge transfer and the electronic properties in organic binary compounds by crystal engineering: a perspective. *J. Mater. Chem. C* **2018**, *6*, 1884−1902.

(38) Han, G.; Yi, Y. Local Excitation/Charge-Transfer Hybridization Simultaneously Promotes Charge Generation and Reduces Non-radiative Voltage Loss in Nonfullerene Organic Solar Cells. *J. Phys. Chem. Lett.* **2019**, *10*, 2911−2918.

(39) Xu, Y.; Yao, H.; Ma, L.; Hong, L.; Li, J.; Liao, Q.; Zu, Y.; Wang, J.; Gao, M.; Ye, L.; et al. Tuning the hybridization of local exciton and charge-transfer states in highly efficient organic photovoltaic cells. *Angew. Chem.* **2020**, *132*, 9089−9095.

(40) Tamura, H.; Burghardt, I. Ultrafast charge separation in organic photovoltaics enhanced by charge delocalization and vibronically hot exciton dissociation. *J. Am. Chem. Soc.* **2013**, *135*, 16364−16367.

(41) Gélinas, S.; Rao, A.; Kumar, A.; Smith, S. L.; Chin, A. W.; Clark, J.; van der Poll, T. S.; Bazan, G. C.; Friend, R. H. Ultrafast long-range charge separation in organic semiconductor photovoltaic diodes. *Science* **2014**, *343*, 512−516.

(42) Yang, B.; Yi, Y.; Zhang, C.-R.; Aziz, S. G.; Coropceanu, V.; Brédas, J.-L. Impact of electron delocalization on the nature of the charge-transfer states in model pentacene/C60 interfaces: a density functional theory study. *J. Phys. Chem. C* **2014**, *118*, 27648−27656.

(43) Bernardo, B.; Cheyns, D.; Verreet, B.; Schaller, R.; Rand, B. P.; Giebink, N. Delocalization and dielectric screening of charge transfer states in organic photovoltaic cells. *Nat. Commun.* **2014**, *5*, 3245.

(44) D'Avino, G.; Muccioli, L.; Olivier, Y.; Beljonne, D. Charge separation and recombination at polymer−fullerene heterojunctions: delocalization and hybridization effects. *J. Phys. Chem. Lett.* **2016**, *7*, 536−540.

(45) Abramavicius, V.; Pranculis, V.; Melianas, A.; Inganäs, O.; Gulbinas, V.; Abramavicius, D. Role of coherence and delocalization in photo-induced electron transfer at organic interfaces. *Sci. Rep.* **2016**, *6*, 32914.

(46) Shen, X.; Han, G.; Yi, Y. The nature of excited states in dipolar donor/fullerene complexes for organic solar cells: evolution with the donor stack size. *Phys. Chem. Chem. Phys.* **2016**, *18*, 15955−15963.

(47) Chen, X.-K.; Ravva, M. K.; Li, H.; Ryno, S. M.; Brédas, J.-L. Effect of molecular packing and charge delocalization on the nonradiative recombination of charge-transfer states in organic solar cells. *Adv. Energy Mater.* **2016**, *6*, 1601325.

(48) Sutton, C.; Tummala, N. R.; Kemper, T.; Aziz, S. G.; Sears, J.; Coropceanu, V.; Brédas, J.-L. Understanding the effects of electronic polarization and delocalization on charge-transport levels in oligoacene systems. *J. Chem. Phys.* **2017**, *146*, 224705.

(49) Gluchowski, A.; Gray, K. L.; Hood, S. N.; Kassal, I. Increases in the charge separation barrier in organic solar cells due to delocalization. *J. Phys. Chem. Lett.* **2018**, *9*, 1359−1364.

(50) Felekidis, N.; Melianas, A.; Kemerink, M. The Role of Delocalization and Excess Energy in the Quantum Efficiency of Organic Solar Cells and the Validity of Optical Reciprocity Relations. *J. Phys. Chem. Lett.* **2020**, *11*, 3563−3570.

(51) Ran, N. A.; Roland, S.; Love, J. A.; Savikhin, V.; Takacs, C. J.; Fu, Y.-T.; Li, H.; Coropceanu, V.; Liu, X.; Brédas, J.-L.; et al. Impact of interfacial molecular orientation on radiative recombination and charge generation efficiency. *Nat. Commun.* **2017**, *8*, 79.

(52) Fazzi, D.; Barbatti, M.; Thiel, W. Hot and Cold Charge-Transfer Mechanisms in Organic Photovoltaics: Insights into the Excited States of Donor/Acceptor Interfaces. *J. Phys. Chem. Lett.* **2017**, *8*, 4727−4734.

(53) Lin, Y. L.; Fusella, M. A.; Rand, B. P. The impact of local morphology on organic donor/acceptor charge transfer states. *Adv. Energy Mater.* **2018**, *8*, 1702816.

(54) Han, G.; Yi, Y.; Shuai, Z. From molecular packing structures to electronic processes: theoretical simulations for organic solar cells. *Adv. Energy Mater.* **2018**, *8*, 1702743.

(55) Lutsker, V.; Aradi, B.; Niehaus, T. A. Implementation and benchmark of a long-range corrected functional in the density functional based tight-binding method. *J. Chem. Phys.* **2015**, *143*, 184107.

(56) Humeniuk, A.; Mitrić, R. Long-range correction for tight-binding TD-DFT. *J. Chem. Phys.* **2015**, *143*, 134120.

(57) Kranz, J. J.; Elstner, M.; Aradi, B.; Frauenheim, T.; Lutsker, V.; Garcia, A. D.; Niehaus, T. A. Time-dependent extension of the long-range corrected density functional based tight-binding method. *J. Chem. Theory Comput.* **2017**, *13*, 1737−1747.

(58) Plasser, F.; Lischka, H. Analysis of excitonic and charge transfer interactions from quantum chemical calculations. *J. Chem. Theor. Comput.* **2012**, *8*, 2777−2789.

(59) Mewes, S. A.; Mewes, J.-M.; Dreuw, A.; Plasser, F. Excitons in poly(para phenylene vinylene): a quantum-chemical perspective based on high-level ab initio calculations. *Phys. Chem. Chem. Phys.* **2016**, *18*, 2548−2563.

(60) Plasser, F. TheoDORE: A toolbox for a detailed and automated analysis of electronic excited state computations. *J. Chem. Phys.* **2020**, *152*, 084108.

(61) Hedström, S.; Tao, Q.; Wang, E.; Persson, P. Rational design of D-A1-D-A2 conjugated polymers with superior spectral coverage. *Phys. Chem. Chem. Phys.* **2015**, *17*, 26677−26689.

(62) Tao, Q.; Xia, Y.; Xu, X.; Hedström, S.; Bäcke, O.; James, D. I.; Persson, P.; Olsson, E.; Inganäs, O.; Hou, L.; et al. D−A1−D−A2 copolymers with extended donor segments for efficient polymer solar cells. *Macromolecules* **2015**, *48*, 1009−1016.

(63) Keshtov, M. L.; Khokhlov, A. R.; Kuklin, S. A.; Chen, F.-C.; Koukaras, E. N.; Sharma, G. D. New D-A1-D-A2-Type Regular Terpolymers Containing Benzothiadiazole and Benzotrithiophene Acceptor Units for Photovoltaic Application. *ACS Appl. Mater. Interfaces* **2016**, *8*, 32998−33009.

(64) Wang, Y.; Kim, S. W.; Lee, J.; Matsumoto, H.; Kim, B. J.; Michinobu, T. Dual Imide-Functionalized Unit-Based Regioregular D−A1−D−A2 Polymers for Efficient Unipolar n-Channel Organic Transistors and All-Polymer Solar Cells. *ACS Appl. Mater. Interfaces* **2019**, *11*, 22583−22594.

(65) Li, P.; Xu, L.; Shen, H.; Duan, X.; Zhang, J.; Wei, Z.; Yi, Z.; Di, C. A.; Wang, S. D-A1-D-A2 Copolymer Based on Pyridine-Capped Diketopyrrolopyrrole with Fluorinated Benzothiadiazole for High-Performance Ambipolar Organic Thin-Film Transistors. *ACS Appl. Mater. Interfaces* **2016**, *8*, 8620−8626.

(66) Wang, Y.; Hasegawa, T.; Matsumoto, H.; Mori, T.; Michinobu, T. D-A1-D-A2 Backbone Strategy for Benzobisthiadiazole Based n-Channel Organic Transistors: Clarifying the Selenium-Substitution Effect on the Molecular Packing and Charge Transport Properties in Electron-Deficient Polymers. *Adv. Funct. Mater.* **2017**, *27*, 1701486.

(67) Aradi, B.; Hourahine, B.; Frauenheim, T. DFTB+, a sparse matrix-based implementation of the DFTB method. *J. Phys. Chem. A* **2007**, *111*, 5678−5684.

(68) Niehaus, T. A. Approximate time-dependent density functional theory. *J. Mol. Struct.* **2009**, *914*, 38−49.

(69) Baer, R.; Neuhauser, D. Density functional theory with correct long-range asymptotic behavior. *Phys. Rev. Lett.* **2005**, *94*, 043002.

(70) Livshits, E.; Baer, R. A well-tempered density functional theory of electrons in molecules. *Phys. Chem. Chem. Phys.* **2007**, *9*, 2932−2941.

(71) Elstner, M.; Porezag, D.; Jungnickel, G.; Elsner, J.; Haugk, M.; Frauenheim, T.; Suhai, S.; Seifert, G. Self-consistent-charge density-functional tight-binding method for simulations of complex materials properties. *Phys. Rev. B: Condens. Matter Mater. Phys.* **1998**, *58*, 7260.

(72) Vuong, V. Q.; Akkarapattiakal Kuriappan, J.; Kubillus, M.; Kranz, J. J.; Mast, T.; Niehaus, T. A.; Irle, S.; Elstner, M. Parametrization and benchmark of long-range corrected DFTB2 for organic molecules. *J. Chem. Theor. Comput.* **2018**, *14*, 115−125.

(73) Elstner, M.; Hobza, P.; Frauenheim, T.; Suhai, S.; Kaxiras, E. Hydrogen bonding and stacking interactions of nucleic acid base pairs: A density-functional-theory based treatment. *J. Chem. Phys.* **2001**, *114*, 5149−5155.

(74) Darghouth, A. A. M. H. M.; Casida, M. E.; Zhu, X.; Natarajan, B.; Su, H.; Humeniuk, A.; Titov, E.; Miao, X.; Mitric, R. Effect of Varying the TD-lc-DFTB Range-Separation Parameter on Charge and Energy Transfer in a Model Pentacene/Buckminsterfullerene Heterojunction. *J. Chem. Phys.* **2021**, *154*, 054102.

(75) Darghouth, A. A. M.; Correa, G. C.; Juillard, S.; Casida, M. E.; Humeniuk, A.; Mitrić, R. Davydov-type excitonic effects on the absorption spectra of parallel-stacked and herringbone aggregates of pentacene: Time-dependent density-functional theory and time-dependent density-functional tight binding. *J. Chem. Phys.* **2018**, *149*, 134111.

(76) Darghouth, A. A. M.; Casida, M. E.; Taouali, W.; Alimi, K.; Ljungberg, M. P.; Koval, P.; Sánchez-Portal, D.; Foerster, D. Assessment of density-functional tight-binding ionization potentials and electron affinities of molecules of interest for organic solar cells against first-principles GW calculations. *Computation* **2015**, *3*, 616−656.

(77) Stojanović, L.; Aziz, S. G.; Hilal, R. H.; Plasser, F.; Niehaus, T. A.; Barbatti, M. Nonadiabatic dynamics of cycloparaphenylenes with TD-DFTB surface hopping. *J. Chem. Theory Comput.* **2017**, *13*, 5846−5860.

(78) Plasser, F. *TheoDORE: a Package for Theoretical Density, Orbital Relaxation, and Exciton Analysis*, version 2.0, 2019; http://theodore-qc.sourceforge.net.

(79) Bloino, J.; Zheng, G.; Sonnenberg, J.; Hada, M.; Ehara, M.; Toyota, K.; Fukuda, R.; Hasegawa, J.; Ishida, M.; Nakajima, T. et al. *Gaussian 09*, Revision D. 01; Gaussian, Inc.: Wallingford, CT, 2009.

(80) Crespo-Otero, R.; Barbatti, M. Spectrum simulation and decomposition with nuclear ensemble: formal derivation and application to benzene, furan and 2-phenylfuran. *Theor. Chem. Acc.* **2012**, *131*, 1237.

(81) Barbatti, M.; Ruckenbauer, M.; Plasser, F.; Pittner, J.; Granucci, G.; Persico, M.; Lischka, H. Newton-X: a surface-hopping program for nonadiabatic molecular dynamics. *Wiley Interdiscip. Rev.: Comput. Mol. Sci.* **2014**, *4*, 26−33.

(82) Barbatti, M.; Granucci, G.; Ruckenbauer, M.; Plasser, F.; Crespo-Otero, R.; Pittner, J.; Persico, M.; Lischka, H. *NEWTON-X: a Package for Newtonian Dynamics Close to the Crossing Seam*, 2018, http://www.newtonx.org.